PCCP

ROYAL SOCIETY OF CHEMISTRY

PAPER

View Article Online
View Journal | View Issue

Check for updates

Cite this: *Phys. Chem. Chem. Phys.*, 2025, **27**, 16336

Computing L- and M-edge spectra using the DFT/CIS method with spin–orbit coupling†

Aniket Mandal ‡ and John M. Herbert *

Modeling L-edge spectra at X-ray wavelengths requires consideration of spin–orbit splitting of the 2p orbitals. We introduce a low-cost tool to compute core-level spectra that combines a spin–orbit mean-field description of the Breit–Pauli Hamiltonian with nonrelativistic excited states computed using the semi-empirical density-functional theory configuration-interaction singles (DFT/CIS) method, within the state-interaction approach. Our version of DFT/CIS was introduced recently for K-edge spectra and includes a semi-empirical correction to the core orbital energies, significantly reducing *ad hoc* shifts that are typically required when time-dependent (TD-)DFT is applied to core-level excitations. In combination with the core/valence separation approximation and spin–orbit couplings, the DFT/CIS method affords semiquantitative L-edge spectra at CIS cost. Spin–orbit coupling has a qualitative effect on the spectra, as demonstrated for a variety of 3d transition metal systems and main-group compounds. The use of different active orbital spaces helps to facilitate spectral assignments. We find that spin–orbit splitting has a negligible effect on M-edge spectra for 3d transition metal species.

Received 2nd May 2025,
Accepted 11th July 2025

DOI: 10.1039/d5cp01656h

rsc.li/pccp

1 Introduction

Near-edge X-ray absorption spectroscopy (XAS) is a powerful technique for investigating the electronic structure of molecules and materials, exhibiting atomic and even oxidation-state specificity. K-edge XAS corresponds to excitations originating from elemental 1s orbitals, the localized nature of which means that XAS serves as a reporter on the valence virtual orbitals.[1–4] This can be used to probe oxidation states[5] and orbital covalency[6–8] in transition-metal bonding. L- and M-edge spectra originate with transitions from 2p and 3p orbitals, respectively, that maintain elemental oxidation-state specificity.[8–17] This is especially useful for analyzing the electronic structure of transition metal compounds.[6,18,19] Probing the valence virtual orbitals enables determination of the local symmetry around a transition metal center,[20–23] and can serve as an indicator for strong correlation effects in the 3d orbitals.[24]

In moving beyond the standard technique of multiplet ligand-field theory,[10,25–27] the biggest obstacle to atomistic *ab initio* simulation of core-level spectra is the high cost of benchmark-quality quantum chemistry methods.[3,28–32] Time-dependent density functional theory (TD-DFT) can be applied to much larger systems,[33–37] and for X-ray spectroscopy it often affords accurate results for peak splittings.[38] However, substantial absolute shifts are typically required in order to match experiment (*e.g.*, ∼20 eV for the L-edge of 3d transition metals),[39] even if these shifts amount to only a few percent of the core-to-valence excitation energies. These shifts are primarily artifacts of differential self-interaction error (SIE) between compact core and delocalized valence orbitals,[40–42] as evidenced by improved results as the fraction of exact exchange is increased.[39,43–45] SIE artifacts are also present in the "real-time" approach to TD-DFT,[35] which is also subject to contamination by continuum states.[35,37,46–48]

To circumvent the need for large empirical shifts, specialized functionals have been developed for core-level spectroscopy,[43,49–52] and modified forms of linear response theory have also been suggested.[53,54] Alternatively, we have reported a new implementation[55] of the so-called DFT/CIS method.[56] This approach uses the formalism of configuration interaction with single substitutions (CIS) but incorporates molecular orbitals (MOs) and one-electron energy levels from Kohn–Sham DFT. A few empirical parameters are used to avoid double-counting of electron correlation effects.[55,56] Our implementation extends the original DFT/CIS method to core-level spectroscopy using the core/valence separation (CVS) approximation.[30,35] An empirical shift of the 1s orbital energies, based on atomic calculations with scalar relativistic corrections, is used to reduce differential SIE effects, with a concomitant reduction in the magnitude of the empirical shifts that are required to reproduce experimental spectra.[55]

In comparison to K-edge XAS, L-edge spectroscopy has several desirable characteristics including greater intensity

---

Department of Chemistry & Biochemistry, The Ohio State University, Columbus, Ohio 43210, USA. E-mail: herbert@chemistry.ohio-state.edu

† Electronic supplementary information (ESI) available: Coordinates of all systems examined. See DOI: **https://doi.org/10.1039/d5cp01656h**

‡ Present address: Dept. of Physics, Rutgers University, Newark, New Jersey USA.

because the most interesting transitions are dipole-allowed (*e.g.*, 2p → 3d),[57] whereas 1s → 3d transitions that also probe metal–ligand covalency appear as relatively weak pre-edge features[58–60] that may be better probed by K-shell fluorescence spectroscopy.[58] L-edge linewidths are reduced due to longer core-hole lifetimes, as compared to K-edge transitions,[10] making L-edge XAS a formidable experimental tool. M-edge spectroscopy at extreme ultraviolet (XUV) wavelengths shares the same selection rules and is now accessible *via* tabletop instruments[61–63] with ultrafast time resolution,[13–16,61–68] providing a sensitive probe of transition metal spin and oxidation states.[69]

Theoretical simulation of L- and M-edge spectra is challenging due to spin–orbit coupling (SOC) that splits the 2p and 3p orbitals into states with $J = 1/2$ or $J = 3/2$.[39,70] The present work extends our new DFT/CIS method to include SOC effects, without further parameterization. Results are presented for a variety of 3d transition metal systems and some main-group compounds, indicating favorable agreement with experiment using only modest empirical shifts.

2 Theory

2.1 DFT/CIS method

The DFT/CIS formalism is similar to that of the CIS method,[37,71] with a few modifications necessitated by the use of Kohn–Sham orbitals. We use $\psi_i, \psi_j, \ldots$ to denote occupied MOs and $\psi_a, \psi_b, \ldots$ for virtual MOs, with indices $r, s, \ldots$ referring to arbitrary (occupied or virtual) MOs. We take these to be eigenfunctions of the Fock operator,

$$\hat{F}\psi_r = \varepsilon_r\psi_r, \tag{1}$$

with orbital energy levels ε_r.

Let $|\Psi_0\rangle$ denote the reference determinant that solves the ground-state self-consistent field (SCF) problem, with ground-state energy E_0. Let $|\Psi_i^a\rangle$ indicate a singly substituted Slater determinant with respect to that reference state. Using a closed-shell formalism for simplicity, diagonal matrix elements of the Hamiltonian in the singly substituted basis are[71]

$$\langle\Psi_i^a|\hat{H}|\Psi_i^a\rangle = E_0 + \varepsilon_a - \varepsilon_i + 2(\psi_i\psi_a|\psi_i\psi_a) - (\psi_i\psi_i|\psi_a\psi_a). \tag{2}$$

The off-diagonal elements are

$$\langle\Psi_i^a|\hat{H}|\Psi_j^b\rangle = 2(\psi_i\psi_a|\psi_j\psi_b) - (\psi_i\psi_j|\psi_a\psi_b). \tag{3}$$

Two-electron integrals in these equations are expressed using Mulliken notation.[71] In the CIS method, Brillouin's theorem ensures that

$$\langle\Psi_0|\hat{H}|\Psi_i^a\rangle = 0. \tag{4}$$

Grimme introduced the first version of DFT/CIS,[56] based on MOs obtained using the B3LYP functional. For that reason, we refer to Grimme's original method as "B3LYP/CIS". In attempting to adapt it for core-level spectroscopy, we found that the parameterization was not appropriate for elements beyond the second row of the periodic table (*i.e.*, beyond Ne). As such, we introduced a new parameterization based on the CAM-B3LYP functional,[72] a range-separated hybrid that is better suited to TD-DFT applications because it mitigates severe underestimation of Rydberg and other charge-transfer transitions.[72–76] We refer to this new parameterization as "CAM-B3LYP/CIS".[55] It was originally parameterized for use with the def2-TZVPD basis set,[77] although the results are not strongly sensitive to that choice and smaller basis sets can be used.[55]

For CAM-B3LYP/CIS we leave eqn (3) and (4) unchanged, following Grimme's prescription,[56] even though Brillouin's theorem is not generally satisfied by Kohn–Sham MOs. However, we modify the diagonal matrix elements in eqn (2) to obtain

$$\langle\Psi_i^a|\hat{H}|\Psi_i^a\rangle = E_0 + \varepsilon_a - \varepsilon_i + 2c_2J_{ia} - c_1K_{ia} - \Delta\varepsilon_i \tag{5}$$

where c_1, c_2, and $\Delta\varepsilon_i$ are empirical parameters (see below) and

$$J_{ia} = (\psi_i\psi_a|\psi_i\psi_a) \tag{6a}$$

$$K_{ia} = (\psi_i\psi_i|\psi_a\psi_a). \tag{6b}$$

These expressions are intended to be used with Kohn–Sham orbitals $\{\psi_r\}$ and energy levels $\{\varepsilon_r\}$. Unlike the analogous TD-DFT linear-response equations,[37] there is no exchange–correlation kernel in the matrix elements defined in eqn (5). Recent work has shown that the effect of this kernel is negligible in core-level TD-DFT calculations.[78] Even for valence excitations, the parameterization of DFT/CIS means that it works well without this kernel.[55,56]

Parameters $c_1 = 0.525$ and $c_2 = 0.850$ in eqn (5) were determined[55] using a subset of QuestDB, a benchmark data set of excitation energies for small and medium-size molecules.[79] The correction $\Delta\varepsilon_i$ in eqn (5) is an overall shift, which is different for the first two rows of the periodic table than it is for heavier atoms. Specifically,[55]

$$\Delta\varepsilon_i = \begin{cases} 0.0250\varepsilon_i & \text{if}\,|\varepsilon_i| \leq 102E_\mathrm{h} \\ 0.0083\varepsilon_i - 1.4209E_\mathrm{h} & \text{if}\,|\varepsilon_i| > 102E_\mathrm{h} \end{cases}. \tag{7}$$

(Note that $\varepsilon_i < 0$.) This was determined in order to shift CAM-B3LYP 1s orbital energies $\{\varepsilon_i\}$ into agreement with those obtained using the short-range corrected (SRC) functional known as SRC1.[43] That functional was specifically parameterized to obtain K-edge spectra with experimental accuracy and uses a large fraction of exact exchange on a very short length scale (<1 Å), in order to reduce SIE for the core states. The correction $\Delta\varepsilon_i$ reduces the inherent errors in core-level eigenvalues obtained from CAM-B3LYP and represents an alternative to shifting spectra to match experiment, as would be required in a XAS calculation using TD-CAM-B3LYP. Absent the $\Delta\varepsilon_i$ correction, 1s energy levels from CAM-B3LYP are less strongly bound as compared to the corresponding SRC1 values and this discrepancy is adjusted *via* eqn (7).

For elements H through Ne, corresponding to $|\varepsilon_i| \leq 102E_\mathrm{h}$, the shift introduced in eqn (7) has essentially the same numerical value as the shift used by Grimme in B3LYP/CIS,[56] despite a rather different parameterization and functional form.[55]

This agreement reflects that fact that core-level eigenvalues from both B3LYP and CAM-B3LYP underestimate excitation energies for XAS by approximately the same amount. However, the CAM-B3LYP/CIS parameterization works for third-row elements ($|\varepsilon_i| > 102E_\mathrm{h}$), whereas Grimme's parameterization does not.

Our choice for the modifications in eqn (5) is motivated by the observation that the majority of the correction in B3LYP/CIS comes from the c_1 parameter. Grimme introduced an alternative form for the shift in $\langle\Psi_i^a|\hat{H}|\Psi_i^a\rangle$ that involves Coulomb integrals and is more difficult to evaluate.[55] This correction was intended to better describe Rydberg and charge-transfer states where the exchange integral K_{ia} is smaller than it is for localized valence excitations. However, the use of a range-separated hybrid functional means that CAM-B3LYP/CIS is inherently better equipped to deal with those types of transitions. Thus, we simplify the form of the empirical shift ($\Delta\varepsilon_i$) by modernizing the DFT functional.

2.2 Spin–orbit coupling

Relativistic effects are present in all core-level spectra but in the context of electronic structure calculations they can be split into two categories: scalar and spin–orbit.[80] The latter do not play a significant role in K-edge spectroscopy because the 1s orbitals are energetically isolated. So long as peak splittings and other spectral features are accurate, K-edge spectra can simply be shifted to account for relativistic effects, using scalar relativistic corrections for the isolated atoms that can be computed, once and for all, across the periodic table.[81–83]

This is not the case for L-edge spectra, however, where SOC splits the triply degenerate 2p orbitals into one $2p_{1/2}$ orbital and two $2p_{3/2}$ orbitals. SOC leads to mixing of spin–orbit-free states with different multiplicities, resulting in two peaks at the L-edge: the L_2 peak (originating from the $2p_{1/2}$ orbital) and the L_3 peak (from the $2p_{3/2}$ orbitals). An analogous splitting of the 3p orbitals is observable in M-edge spectroscopy.

SOC effects can be incorporated using either variational or perturbative methods.[80] Variational treatments include the zeroth-order regular approximation (ZORA),[84] the Douglass–Kroll–Hess (DKH) method,[85] and the exact two-component (X2C) approach.[86] These methods incorporate spin–orbit operators into the wave function optimization, which is the formally more rigorous approach and is necessary when SOC effects become sufficiently large. However, variational treatment of SOC adds significantly to the complexity of the formalism and increases the computational cost by perhaps an order of magnitude, relative to a nonrelativistic calculation.[87] Perturbative treatment of SOC is more affordable and is sufficiently accurate for the first few rows of the periodic table.[88] This approach, which is the one adopted here, involves construction of the Breit–Pauli Hamiltonian using nonrelativistic (spin–orbit-free) wave functions as basis states.

2.2.1 Breit–Pauli Hamiltonian.

We incorporate SOC as off-diagonal coupling matrix elements between eigenstates of the nonrelativistic (Coulomb electronic) Hamiltonian, in what has been called the "state-interaction" approach.[89] In the present work, the nonrelativistic basis states are obtained from DFT/CIS calculations that include a large number of singlet and triplet core-excited states. We denote the DFT/CIS or TD-DFT state energies as $E(\mathrm{S}_n)$ for the singlet state S_n and $E(\mathrm{T}_n^{(M)})$ for the triplet state T_n, with multiplet components ($M \in \{-1, 0, +1\}$) that are degenerate in the DFT/CIS calculations:

$$E(\mathrm{T}_n^{(-1)}) = E(\mathrm{T}_n^{(0)}) = E(\mathrm{T}_n^{(+1)}). \tag{8}$$

Within the state-interaction picture, the Breit–Pauli Hamiltonian incorporates SOC between the aforementioned spin–orbit-free basis states, and can be written in matrix form as

$$\mathbf{H}_\mathrm{BP} = \begin{pmatrix} E(\mathrm{S}_0) & 0 & \cdots & V(\mathrm{S}_0, \mathrm{T}_n^{(-1)}) & V(\mathrm{S}_0, \mathrm{T}_n^{(0)}) & V(\mathrm{S}_0, \mathrm{T}_n^{(+1)}) \\ 0 & E(\mathrm{S}_1) & \cdots & V(\mathrm{S}_1, \mathrm{T}_n^{(-1)}) & V(\mathrm{S}_1, \mathrm{T}_n^{(0)}) & V(\mathrm{S}_1, \mathrm{T}_n^{(+1)}) \\ \vdots & \vdots & \ddots & \vdots & \vdots & \vdots \\ V(\mathrm{T}_n^{(-1)}, \mathrm{S}_0) & V(\mathrm{T}_n^{(-1)}, \mathrm{S}_1) & \cdots & E(\mathrm{T}_n^{(-1)}) & 0 & 0 \\ V(\mathrm{T}_n^{(0)}, \mathrm{S}_0) & V(\mathrm{T}_n^{(0)}, \mathrm{S}_1) & \cdots & 0 & E(\mathrm{T}_n^{(0)}) & 0 \\ V(\mathrm{T}_n^{(+1)}, \mathrm{S}_0) & V(\mathrm{T}_n^{(+1)}, \mathrm{S}_1) & \cdots & 0 & 0 & E(\mathrm{T}_n^{(+1)}) \end{pmatrix}. \tag{9}$$

In principle, one might add scalar relativistic corrections to the diagonal matrix elements in $\mathbf{H}_\mathrm{BP}$. For the $L_{2,3}$-edges of silicon and sulfur, such corrections are smaller than 0.05 eV.[81] For 3d transition metals considered here, these corrections range from 0.6–2.1 eV,[81] which is small compared to shifts that are applied to match experiment.

Off-diagonal matrix elements $V(\mathrm{T}_n^{(M)}, \mathrm{S}_m)$, containing the SOC interaction between spin–orbit-free states $\mathrm{T}_n^{(M)}$ and S_m, are evaluated here using the spin–orbit mean-field (SOMF) approximation.[90,91] These couplings are matrix elements of the Breit–Pauli spin–orbit operator,[32,90–95]

$$\hat{H}_\mathrm{SO} = \frac{\alpha}{2}\sum_{k}^{\mathrm{elec}}\left[\hat{\mathbf{h}}_k^{\mathrm{sso}}\cdot\hat{\mathbf{s}}_k - \sum_{l\neq k}^{\mathrm{elec}}\hat{\mathbf{h}}_{k,l}^{\mathrm{soo}}\cdot(\hat{\mathbf{s}}_k + 2\hat{\mathbf{s}}_l)\right]. \tag{10}$$

Here, α is the fine-structure constant and $\hat{\mathbf{s}}_k$ is the spin angular momentum for electron k. The one-electron operator $\hat{\mathbf{h}}_k^{\mathrm{sso}}$ in eqn (10) is the "spin–same-orbit" coupling, given by

$$\hat{\mathbf{h}}_k^{\text{sso}} = \sum_K^{\text{nucl}} \frac{Z_K(\mathbf{r}_k - \mathbf{R}_K) \times \mathbf{p}_k}{\|\mathbf{r}_k - \mathbf{R}_K\|^3} \tag{11}$$

where $\mathbf{r}_k$ and $\mathbf{R}_K$ are the coordinates of electron k and nucleus K, respectively, with the latter having atomic number Z_K. One may recognize $(\mathbf{r}_k - \mathbf{R}_K) \times \mathbf{p}_k$ in eqn (11) as the orbital angular momentum about nucleus K. The two-electron operator $\hat{\mathbf{h}}_{k,l}^{\text{soo}}$ in eqn (10) represents "spin–other-orbit" coupling,

$$\hat{\mathbf{h}}_{k,l}^{\text{soo}} = \frac{(\mathbf{r}_k - \mathbf{r}_l) \times \mathbf{p}_l}{\|\mathbf{r}_k - \mathbf{r}_l\|^3}. \tag{12}$$

This form invokes the SOMF approximation,[32,90–95] which simplifies calculation of the coupling matrix elements insofar as explicit two-electron integrals are not required. Within this approximation, matrix elements of $\hat{H}_{\text{SO}}$ can be evaluated using only one-electron integrals and transition density matrices.[95]

The formalism introduced above can be used with either DFT/CIS or TD-DFT.[95] Matrix elements $\langle \Psi(S, M_S)|\hat{H}_{\text{SO}}|\Psi'(S', M'_S)\rangle$ in the basis of nonrelativistic states afford the off-diagonal terms in the matrix $\mathbf{H}_{\text{BP}}$. In the present work, these states are either singlets ($S = 0 = M_S$) or triplets ($S = 1$ and $M_S \in \{-1, 0, +1\}$). Diagonalization of $\mathbf{H}_{\text{BP}}$ in eqn (9) affords the coupled target states.

2.2.2 Oscillator strengths. To compute spectra we need oscillator strengths for the coupled states. We start from the transition dipole moments in the nonrelativistic basis, which have the form

$$\mu^{\alpha}_{S,M_S;S',M'_S} = \langle \Psi(S, M_S)|\hat{\mu}_{\alpha}|\Psi'(S', M'_S)\rangle \tag{13}$$

where $\alpha \in \{x, y, z\}$ and $\hat{\mu}_{\alpha} = e\hat{\alpha}$ is the α component of the dipole moment operator. Suppressing the spin quantum numbers (S, M_S) for brevity, the states $|\Psi\rangle$ and $|\Psi'\rangle$ in eqn (13) range over the SCF ground state $|\Psi_0\rangle$ and all of the DFT/CIS or TD-DFT excited states. Each of the excited states is a CIS-style linear combination of singly substituted Slater determinants,

$$|\Psi\rangle = \sum_{ia} x_{ia}|\Psi_i^a\rangle. \tag{14}$$

This is reminiscent of the Tamm–Dancoff approximation (TDA) in TD-DFT,[37,96] which is implicit in the DFT/CIS approach. The requisite matrix elements in eqn (13) are evaluated using the Slater–Condon rules, in what has been called a "pseudo-wave function" approach to computing transition dipole moments between TD-DFT excited states.[97–100] This treatment is consistent with how the Breit–Pauli Hamiltonian has long been used in TD-DFT calculations.[101–103] Formally speaking, state-to-state transition dipoles require quadratic rather than linear response theory,[100,104] but the pseudo-wave function method is consistent with invocation of the TDA.

The nonrelativistic transition dipole moments in eqn (13) vanish if $S \neq S'$, and they are identical for all values of M_S within a given spin multiplet. However, we retain the indices M_S and M'_S in eqn (13) to clarify that the dimension of the matrix $\boldsymbol{\mu}^{\alpha}$ matches the dimension of $\mathbf{H}_{\text{BP}}$. The former can then be transformed into the coupled SOMF basis, using the matrix $\mathbf{U}_{\text{BP}}$ that diagonalizes $\mathbf{H}_{\text{BP}}$:

$$\tilde{\boldsymbol{\mu}}^{\alpha} = \mathbf{U}_{\text{BP}}^{\dagger}\boldsymbol{\mu}^{\alpha}\mathbf{U}_{\text{BP}}. \tag{15}$$

The matrix $\tilde{\boldsymbol{\mu}}^{\alpha}$ contains the α components of the transition dipole moments between SOC states, including the ground state. The oscillator strength for $|0\rangle \to |n\rangle$ excitation, from the ground state to coupled state $|n\rangle$, is given by[37]

$$f_{0\to n} = \frac{2m_{\text{e}}(E_n - E_0)}{3e^2\hbar^2} \sum_{\alpha\in\{x,y,z\}} \left(\tilde{\mu}^{\alpha}_{0,n}\right)^2. \tag{16}$$

3 Computational details

3.1 Implementation

The DFT/CIS method has been implemented in the Q-Chem program,[105] and is available starting from v. 6.2.[55] SOC matrix elements have been implemented in Q-Chem by Krylov and co-workers;[32,92–95] see ref. 95 for the TD-DFT implementation.

Core-level spectra without SOC are computed using either DFT/CIS or TD-DFT within the CVS approximation.[35] Subsequently, in a post-processing step, these spin–orbit-free states are transformed to the coupled basis by diagonalizing $\mathbf{H}_{\text{BP}}$ in eqn (9). For this, we have written a Python code called pySETSOC.[106] This program extracts SOC terms from the Q-Chem output, along with state-to-state transition dipole moments that are computed within the pseudo-wave function approach. It then constructs and diagonalizes $\mathbf{H}_{\text{BP}}$ and computes oscillator strengths for the coupled states. The pySETSOC program can be applied to Q-Chem outputs from TD-DFT or DFT/CIS, using the pseudo-wave function approximation to evaluate the requisite state-to-state transition dipole matrix elements as discussed in Section 2.2.2. The pySETSOC program will also read the output from restricted active-space (RAS)-CI methods,[94,107] although that functionality is not used here.

Finally, spectra are plotted using either Lorentzian or Gaussian broadening. The former is probably more appropriate for core-level spectra that are subject to lifetime broadening arising from the core hole. In many cases, we use a Lorentzian function with a full width at half-maximum (FWHM) of 0.3 eV. Although chosen empirically, this is roughly consistent with 2p core-hole states having natural line widths of ∼0.1 eV.[108,109]

3.2 Core/valence separation

The CVS approximation extends standard excited-state methods to core-level states by eliminating the amplitudes x_{ia} [eqn (14)] associated with all but a small number of occupied MOs, ψ_i.[33–35] This dramatically reduces computational cost by eliminating valence excited states, so that core-to-valence excitations appear as the lowest energy states in the spectrum. Furthermore, the CVS approximation decouples these states from the continuum, which is otherwise problematic (*e.g.*, in real-time approaches).[35,37] Finally, the CVS approximation enables separation of K-, L-, and M-edge spectra in cases where different elemental edges might overlap with one another.

In such situations, peak assignments can be made by comparing DFT/CIS or TD-DFT spectra using different active-space approximations.

All calculations reported here invoke the CVS approximation, which affords negligible errors for K- and L-edge spectra.[32,110] For the L-edge spectra presented here, the occupied orbital active space consists of the 2p orbitals for the element in question along with the entire virtual space. In molecules containing more than one atom with the same atomic number, we include all of the 2p orbitals for that element. M-edge spectra are computed using the analogous procedure with 3p orbitals in the active space. For most calculations, we use 200 singlet and 200 triplet (nonrelativistic) basis states to construct $\mathbf{H}_{\mathrm{BP}}$.

Conventional TD-DFT calculations reported here also use the CVS approximation as well as the TDA. This is consistent with the CIS-style matrix elements used in DFT/CIS, and with the CIS-style pseudo-wave function method that is used to compute oscillator strengths. Previous work suggests that the TDA has a negligible effect on core-level spectra.[35,111]

3.3 Functionals and basis sets

DFT/CIS calculations were performed using CAM-B3LYP,[72] for which the method was parameterized in previous work.[55] The B3LYP-based parameterization introduced by Grimme is not used here, because CAM-B3LYP/CIS is more suitable for computing core-level spectra.

As a point of comparison, conventional TD-DFT calculations are reported using the functionals B3LYP, CAM-B3LYP,[72] and SRC1-r2.[33,43] The latter is specifically parameterized for K-edge spectra of third-row elements, using a large fraction of exact exchange (87%) on a very short length scale ($\lesssim 1$ Å). Although TD-SRC1 is quite accurate for K-edge spectra,[33,35,43,52] it has not yet been tested for L-edge spectra.

CAM-B3LYP/CIS parameters were developed based on calculations using def2-TZVPD.[77] That basis set should be sufficient to converge TD-DFT excitation energies,[37,112–116] but in fact CAM-B3LYP/CIS provides satisfactory results in smaller basis sets also.[55] Except where specified otherwise, the def2-TZVPD basis set is used for all calculations.

4 Results and discussion

4.1 Functional and basis-set effects

The effect of exact exchange on K-edge TD-DFT calculations is well documented,[39,43–45] with larger fractions generally affording more accurate results in the sense that smaller absolute shifts are required. This is primarily due to larger SIE associated with the compact 1s orbital, as compared to the relatively delocalized valence virtual orbitals. Core-to-valence excitations can also be considered to manifest a certain type of charge transfer, whose excitation energy is dramatically underestimated by functionals that lack correct asymptotic behavior.[37,117–119] Although the latter problem is ameliorated as the fraction of exact exchange is increased, this must be balanced against a semilocal correlation functional that is not designed for fully nonlocal Hartree–Fock exchange. Accuracy may be significantly degraded when the fraction of exact exchange rises above 50%.[120] Besley and co-workers solved this problem by introducing SRC functionals with unusually large fractions of exact exchange (>50%) on very short length scales.[43] The range-separation scheme and the fractions of exact exchange that are used in these SRC functionals were determined in order to match experimental K-edge excitation energies and these functionals have not previously been examined for L-edge spectra.

Fig. 1 presents conventional TD-DFT results for the Ti $L_{2,3}$-edge spectrum of $TiCl_4$ using several different functionals, in comparison to CAM-B3LYP/CIS calculations and to experiment.[121] All calculations include SOC so that distinct L_2 and L_3 edges are apparent, separated by ~12 eV. Conventional TD-B3LYP and TD-CAM-B3LYP calculations underestimate the 2p → valence excitation energies by ~15 eV, while CAM-B3LYP/CIS and TD-SRC1-r2 underestimate them by only 5.0 eV (TD-SRC1-r2) or 6.8 eV (CAM-B3LYP/CIS). The fact that all four methods underestimate the excitation energies with respect to experiment suggests that differential SIE remains significant even for the 2p orbitals. Note that the core orbital correction $\Delta\varepsilon_i$ that is used in CAM-B3LYP/CIS was parameterized using 1s orbital energies yet continues to work reasonably well for excitations from the 2p orbitals, as we observed previously.[55]

Notably, relative intensities of L_2 *versus* L_3 are different between theory and experiment. The same artifact has been noted previously in real-time TD-DFT calculations of the same spectrum.[122] Correct intensities are obtained using the ZORA

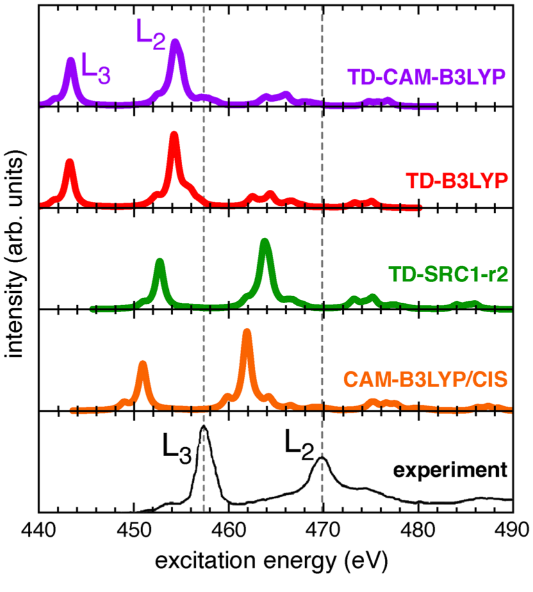

Fig. 1 Direct relation between the accuracy of TD-DFT calculations and the fraction of exact exchange, for Ti $L_{2,3}$-edge spectra of $TiCl_4$. Shown are four different TD-DFT approaches along with CAM-B3LYP/CIS, in comparison to an experimental spectrum from ref. 121. All calculations used the def2-TZVPD basis set and include 200 singlet and 200 triplet basis states. Individual transitions were broadened using a Lorentzian function with FWHM = 0.3 eV.

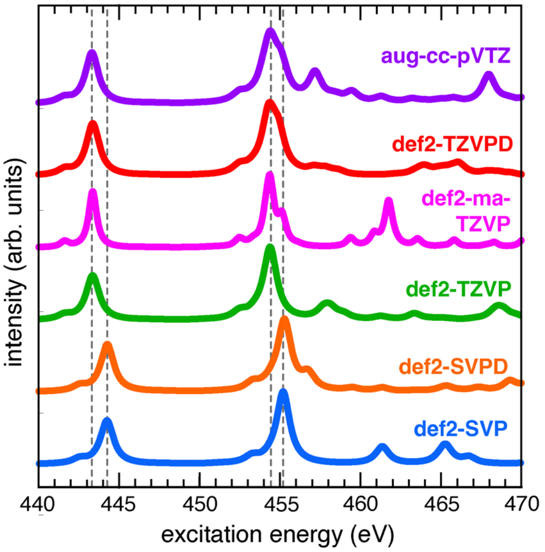

Fig. 2 Basis set effects on the Ti $L_{2,3}$-edge spectrum of $TiCl_4$, computed at the CAM-B3LYP/CIS + SOC level as described in Fig. 1. Spectra are normalized separately so that the main feature (around 455 eV) has the same intensity in each case. Vertical dashed lines are guides to the eye, aligned with the most intense L_2 and L_3 features at the top and at the bottom.

method in conjunction with relativistic basis sets,[123,124] pointing to a limitation of the present approach.

Fig. 2 documents basis-set effects on this $TiCl_4$ spectrum. The position of both the L_2 and L_3 peaks is unchanged amongst the def2-TZVP, def2-TZVPD and aug-cc-pVTZ basis sets. A shoulder on the higher-energy side of the L_2 peak becomes progressively more pronounced as one goes from def2-SVPD to def2-TZVPD to aug-cc-pVTZ, but is absent when diffuse functions are omitted. The minimally augmented def2-ma-TZVP basis set,[125] which removes higher angular momentum diffuse functions from def2-TZVPD, exaggerates the peak splitting near 455 eV and predicts inconsistent intensities at higher energies, as compared to other basis sets. This suggests a role for the diffuse d functions that are present in def2-TZVPD and aug-cc-pVTZ, at least when it comes to lineshapes.

Peak excitation energies are a different matter. Using double-ζ rather than triple-ζ basis sets introduces a shift of about 1 eV in both the L_2 and L_3 features but the $L_{2,3}$ splitting is essentially identically in all of the basis sets tested, as documented in Table 1. In our view, 1 eV shifts in the absolute excitation energies are of no consequence at X-ray wavelengths, where the empirical shifts required to match experiment are 5–7 eV at a minimum. Thus, smaller basis seem to suffice for excitation energies, even while converged lineshapes require diffuse functions.

Table 1 Basis set effects for CAM-B3LYP/CIS + SOC calculations at the Ti $L_{2,3}$-edge of $TiCl_4$

Basis	Exc. energy (eV)		Splitting (eV)
	L_3	L_2	
def2-SVP	444.2	455.2	11.0
def2-SVPD	444.2	455.3	11.0
def2-TZVP	443.4	454.4	11.0
def2-ma-TZVP	443.4	454.4	11.0
def2-TZVPD	443.4	454.4	11.0
aug-cc-pVTZ	443.3	454.4	11.1

4.2 Benchmarking $L_{2,3}$ energies

Fig. 3 shows experimental X(2p) → valence excitation spectra for $TiCl_4$,[121] $SiCl_4$,[126] and CrO_2Cl_2,[127] at the $L_{2,3}$-edge of the central atom (X = Ti, Si, or Cr), along with CAM-B3LYP/CIS + SOC calculations. Splitting of the $L_{2,3}$ features is rather dramatic for $TiCl_4$ (Fig. 3a), highlighting the fact that a spin–orbit-free spectrum contains only one bright feature and is qualitatively incorrect. Additional features in the $L_{2,3}$ spectrum correspond to splitting of the 3d orbitals into t_2 and e sets. Even with SOC, however, intensities of the L_2 and L_3 peaks are inverted relative to experiment, as noted in Section 4.1.

Spectra of $SiCl_4$ at the Si $L_{2,3}$-edge are more complicated (Fig. 3b). One explanation is that the Si(2p) orbitals are less localized as compared to Ti(2p) orbitals, and thus undergo more mixing with the ligand orbitals. Splitting of the Si($2p_{3/2}$) and Si($2p_{1/2}$) features is very small,[126] hence the difference between SOC and nonrelativistic spectra is not as striking in this case as it was for $TiCl_4$. For CrO_2Cl_2 (Fig. 3c), inclusion of SOC is once again necessary to obtain a spectrum that is even qualitatively correct. The L_2 and L_3 edges are well separated, as they were in $TiCl_4$, and the low symmetry C_{2v} environment leads to distinctive peak shapes.

Overall, the Breit–Pauli formalism, combined with the SOMF approximation, works rather well for reproducing the L-edge spectra of these third-row elements. Spectral features contain important information about the nature of the valence virtual orbitals that can be connected to features in the experimental spectra by means of the DFT/CIS + SOC calculations.

Table 2 compares the accuracy of CAM-B3LYP/CIS and conventional TD-DFT, with SOC included in either case and compared to experimental transition energies.[121,126–131] CIS + SOC results are also tabulated, in order to set a baseline. These L-edge results follow the same trend as the K-edge values that we reported previously.[55] Specifically, both the TD-B3LYP and TD-CAM-B3LYP methods underestimate the excitation energies in all cases. This indicates that range separation alone is insufficient to correct the excitation energies, as the errors originate in 2p eigenvalues that are insufficiently bound. The TD-SRC1-r2 method performs better, despite being parameterized for main-group K-edge spectra, because the large fraction of exact exchange at ultrashort range mitigates the eigenvalue problem to some extent. Finally, CAM-B3LYP/CIS + SOC exhibits a mean absolute error (MAE) that is very similar to TD-SRC1-r2 + SOC. This is expected since the $\Delta\varepsilon_i$ correction in the former was based on SRC1-r2 orbital energies.

Mean errors in Table 2 provide an additional indication as to the source of the errors. The CIS method, for example, is SIE-free but lacks complete orbital relaxation and as a result the errors are strictly positive, with a mean error of 10.6 eV. On the other hand, the TD-B3LYP and TD-CAM-B3LYP errors are

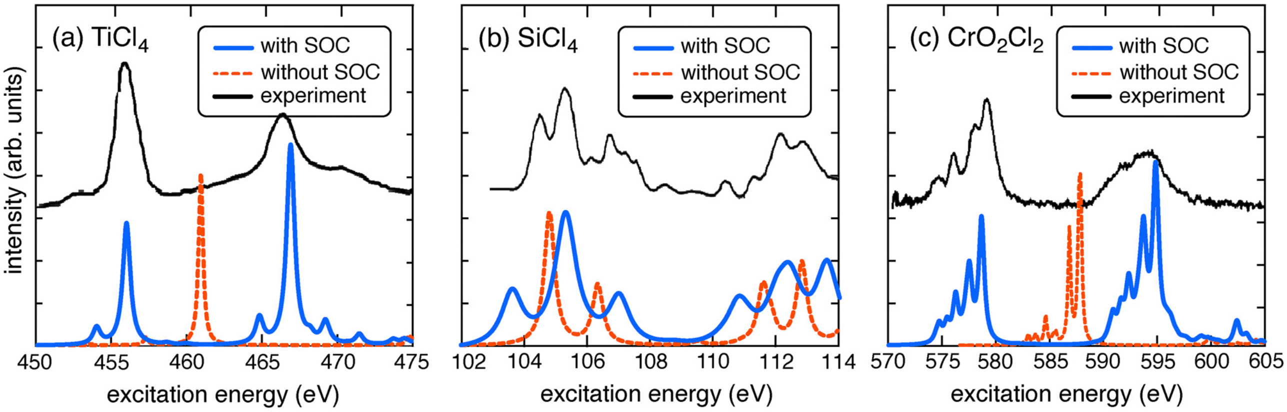

Fig. 3 Experimental $L_{2,3}$-edge spectra for (a) Ti in $TiCl_4$,[121] (b) Si in $SiCl_4$,[126] and (c) Cr in CrO_2Cl_2,[127] in comparison to CAM-B3LYP/CIS + SOC calculations. The latter employ the def2-TZVPD basis set with 200 singlet and 200 triplet excited states. Calculated transition energies were broadened using a Lorentzian function (FWHM = 0.3 eV) and shifted by (a) 5.0 eV, (b) 3.2 eV, and (c) 4.8 eV.

Table 2 Simulated $L_{2,3}$ excitation energies in comparison to experimental values[a]

			Errors in computed values (eV)				
			CIS		TD-DFT		
Molecule	Edge[b]	Expt. (eV)	Standard[c]	DFT/CIS[d]	SRC1-r2	CAM-B3LYP	B3LYP
$SiCl_4$	L_3	104.3[e]	6.8	−3.2	−3.9	−5.3	−5.6
	L_2	104.9[e]	6.5	−2.6	−3.3	−4.6	−5.0
H_2S	L_3	164.9[f]	7.9	−3.4	−1.7	−4.4	−5.0
	L_2	166.5[f]	8.7	−2.6	0.6	−2.2	−3.0
Ar	L_3	244.5[g]	12.0	−0.7	−1.4	−6.7	−6.7
	L_2	246.4[g]	14.2	0.5	1.0	−4.4	−4.5
$TiCl_4$	L_3	457.7[h]	6.7	−6.8	−5.0	−14.3	−14.5
	L_2	462.8[h]	13.0	−0.9	0.9	−8.5	−8.6
VO_4^{3-}	L_3	518.2[i]	6.8	−7.9	−5.4	−16.0	−15.9
	L_2	525.1[i]	13.8	−1.5	1.1	−9.6	−9.2
CrO_2Cl_2	L_3	577.2[j]	11.8	−3.4	−2.0	−13.9	−14.0
	L_2	585.9[j]	19.7	4.0	5.6	−6.6	−6.5
MnO_4^-	L_3	645.6[i]	9.5	−6.9	−5.3	−18.8	−18.8
	L_2	656.0[i]	18.6	2.0	3.9	−9.6	−9.7
$Fe(Cp)_2$	L_3	709.1[k]	1.5	−10.4	−7.9	−22.6	−22.3
	L_2	722.2[k]	11.8	−0.3	2.2	−12.5	−12.2
Mean error			10.6	−2.8	−1.3	−10.0	−10.1
MAE[l]			10.6	3.6	3.2	10.0	10.1

[a] All calculations use def2-TZVPD. [b] L_2 or L_3 for the central atom. [c] Conventional CIS. [d] CAM-B3LYP/CIS. [e] Ref. 126. [f] Ref. 129. [g] Ref. 128. [h] Ref. 121. [i] Ref. 131. [j] Ref. 127. [k] Ref. 130. [l] Mean absolute error.

strictly negative, indicating that SIE dominates over orbital relaxation error. The TD-SRC1-r2 approach, which balances these errors (by virtue of its parameterization using experimental data),[54] exhibits errors of either sign. The same is true of CAM-B3LYP/CIS.

Table 3 lists the $L_{2,3}$ splitting $[\Delta E(L_2) - \Delta E(L_3)]$ from Table 2, along with the error in this splitting as computed using each of the methods examined here. In many cases, the errors are of the same order of magnitude as the experimental splitting itself. Errors are also roughly independent of the theoretical method used, averaging about 5 eV but increasing in magnitude as the splitting itself increases. This means that TD-SRC1-r2 is no more accurate than other TD-DFT methods that weren't parameterized to remove the need for absolute shifts, and furthermore the accuracy of CIS is quite similar. (This is not altogether unexpected, as it speaks to the rather small electron correlation effects on the SOC values, consistent with the accuracy of the SOMF approximation.[90,132,133]) While the origin of the discrepancies in $L_{2,3}$ splittings with respect to experiment are unclear, it seems that they have more to do with the treatment of SOC than with the description of electron correlation.

4.3 CVS as a diagnostic tool

The CVS approximation is needed to extend CIS-type methods to core-level excitations, because it removes valence excitations that appear at lower transition energies so that core-to-valence transitions can be obtained using reasonable subspace sizes in the iterative eigensolver.[35] By performing several calculations with different active occupied orbitals, the CVS approximation

Table 3 Errors in $L_{2,3}$ splittings in comparison to experimental values[a]

		Error (eV)				
				TD-DFT		
Molecule	Expt.[b] (eV)	CIS	DFT/CIS[c]	SRC1-r2	CAM-B3LYP	B3LYP
$SiCl_4$	0.6	0.3	0.6	0.6	0.7	0.6
H_2S	1.6	0.8	0.8	2.3	2.2	2.0
Ar	1.9	2.2	1.2	2.4	2.3	2.2
$TiCl_4$	5.1	6.3	5.9	5.9	5.8	5.9
VO_4^{3-}	6.9	7.0	6.5	6.5	6.4	6.8
CrO_2Cl_2	8.7	7.9	7.4	7.6	7.3	7.5
MnO_4^-	10.4	9.1	8.9	9.2	9.2	9.1
$Fe(Cp)_2$	13.1	10.3	10.1	10.1	10.1	10.1
Mean		5.5	5.2	5.6	5.5	5.5

[a] All calculations use def2-TZVPD. [b] $L_{2,3}$ splitting for the central atom, equal to the difference between experimental L_2 and L_3 values from Table 2. [c] CAM-B3LYP/CIS.

also facilitates separation of the K-, L-, and M-edges of different elements. This is a useful feature because overlapping edges can otherwise make it difficult to assign peaks. The vanadate ion (VO_4^{3-}) affords an example, insofar as the O(1s) K-edge and the V(2p) L-edge are quite close in energy as shown in Fig. 4.

For this small ion, it is possible to perform the calculations without invoking the CVS approximation by computing both valence and core excitations. Upon doing so, subtle dipole-forbidden pre-edge features appear whose origin might at first be unclear. For that matter, given the magnitude of the shifts that are needed to match experiment, it is not clear *a priori* which features in the "no CVS" spectrum in Fig. 4 even correspond to the oxygen K-edge. Using active-space approximations involving only the O(1s) or V(2p) orbitals, these features are readily assignable and it is clear that the oxygen K-edge appears at 529 eV. Moreover, the close resemblance of the V(2p) spectrum and the exact linear-response result (sans CVS approximation) suggests there is little mixing between O(1s) and V(2p) orbitals in the ground state of VO_4^{3-}.

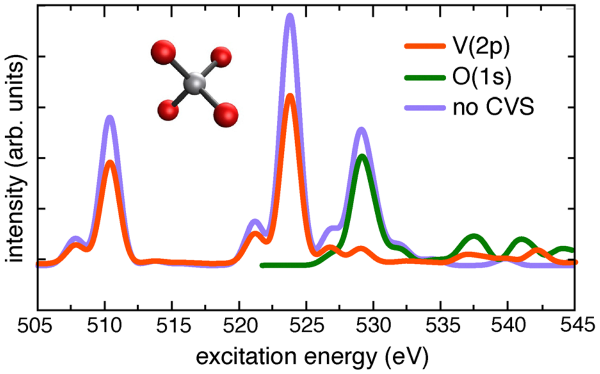

Fig. 4 XAS of VO_4^{3-}, illustrating the important role of the CVS approximation in assigning spectral features. All calculations were performed at the CAM-B3LYP/CIS + SOC level using the def2-TZVPD basis set, including 100 singlet and 100 triplet states broadened with a Lorentzian function (FWHM = 0.3 eV). The calculations labeled V(2p) and O(1s) employ the indicated active occupied orbitals, whereas the "no CVS" calculation uses all MOs. For clarity, the three spectra are normalized separately.

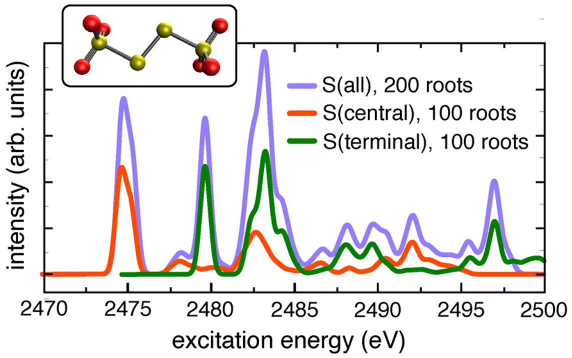

Fig. 5 XAS of $(S_4O_6)^{2-}$ at the sulfur K-edge, illustrating how calculations with different active spaces can be used to assign spectral features. Spectra were computed using CAM-B3LYP/CIS + SOC with the def2-TZVPD basis set and Lorentzian broadening (FWHM = 0.3 eV). CVS active spaces contain S(1s) orbitals on the atoms indicated in the legend.

The CVS approximation can also be a helpful tool when the same element appears more than once in a molecule, in different coordination environments. An example is the tetrathionate ion, $(S_4O_6)^{2-}$, whose terminal sulfur atoms have formal charges of +5 whereas the two interior sulfur atoms have formal charges of zero. Simulated K-edge spectra for this species are shown in Fig. 5 using three different CVS active spaces, consisting of either the S(1s) orbitals on the terminal sulfur atoms, or those on the interior sulfur atoms, or both. The latter spectrum is the true K-edge result but the other two spectra aid in assigning features. These spectra clearly demonstrate how the interior S^0 atoms give rise to lower-energy XAS features as compared to the terminal S^{5+} atoms, which is expected due to the stronger electron–hole interaction when the formal charge is larger.

Note that this decomposition is not exact, in the sense that the sum of the spectra with limited active spaces need not equal the spectrum that is obtained with the union of these active spaces, which is evident from the feature at 2475 eV in Fig. 5. These discrepancies arise due to coupling between S(1s) orbitals on different atoms, when such coupling is available within the active space. Despite their approximate nature, however, such decompositions can be useful diagnostic tools to understand the origins of various spectral features.

Fig. 6 shows the analogous decomposition of the L-edge spectrum of $(S_4O_6)^{2-}$. Here, we use the S(2p) orbitals on either the terminal or the interior sulfur atoms (or both) as the CVS active space, and these calculations once again demonstrate how the lower-energy features originate in transitions localized on the interior S^0 atoms. The approximate nature of the decomposition is evident in some of the features above 165 eV in Fig. 6a. When a significantly larger number of nonrelativistic states is used, spectral features fill in at higher energies (Fig. 6b). The larger calculation is significantly more expensive because it requires computing 800 DFT/CIS singlet states, including state-to-state transition moments between them, then another 800 triplet states and SOC couplings between the singlet and triplet states. The total dimension of

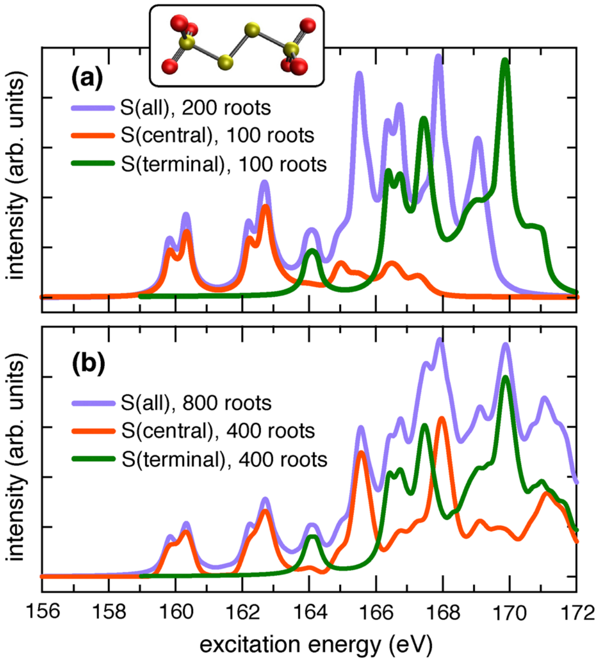

Fig. 6 XAS of $(S_4O_6)^{2-}$ at the sulfur L-edge. All calculations were performed using CAM-B3LYP/CIS + SOC with def2-TZVPD, computing either (a) 200 or (b) 800 singlet and triplet excited states, which were then broadened using a Lorentzian function (FWHM = 0.2 eV). Spectra labeled S(terminal) and S(central) employ only the S(2p) orbitals on the indicated atoms, with a correspondingly smaller number of excited states, whereas S(all) uses all of the S(2p) orbitals.

$\mathbf{H}_{\mathrm{BP}}$ in eqn (9) is 3200 states. Nevertheless, such a calculation is feasible at the DFT/CIS level using the high-quality def2-TZVPD basis set. At the same time, even an approximate decomposition using atom-specific active spaces can be a useful diagnostic and interpretative tool.

4.4 Miscellaneous L-edge applications

We next consider a variety of applications of CAM-B3LYP/CIS + SOC to compute L-edge spectra of main-group compounds and transition metal complexes.

4.4.1 L-edge spectra of SF_6. XAS of SF_6 at the S(2p) L-edge is considered in Fig. 7, juxtaposing the CAM-B3LYP/CIS spectrum with an experimental one.[134] Peaks labeled 1 and 2, in the region from 172–175 eV, are assigned as a_{1g} symmetry and correspond to excitation of S($2p_{3/2}$) and S($2p_{1/2}$) electrons into the lowest unoccupied MO (LUMO). As compared to those features, peaks 3 and 4 (representing transitions into t_{2g} orbitals) are much more intense, in both the computed and the experimental spectrum, although peak 3 has a doublet structure in the CAM-B3LYP/CIS calculation that is not evident in the experiment. Weaker doublet peaks 5 and 6, representing transitions into a second set of t_{2g} orbitals, are not observed experimentally although they have been observed in real-time TD-DFT calculations.[46] Finally, peaks 7 and 8 in the simulated spectrum correspond to transitions with e_g symmetry. These features are narrow and intense whereas the corresponding region of the experimental spectrum is broad and diffuse.

Some Rydberg states between 179–182 eV are highlighted in an inset to Fig. 7. These appear at slightly higher energies as compared to the Rydberg features identified in the experimental spectrum, from 177–180 eV and identified as a_{1g}, e_g and t_{2g} transitions.[134] Only two peaks can be discerned in the highlighted region of the CAM-B3LYP/CIS spectrum. Ruud and

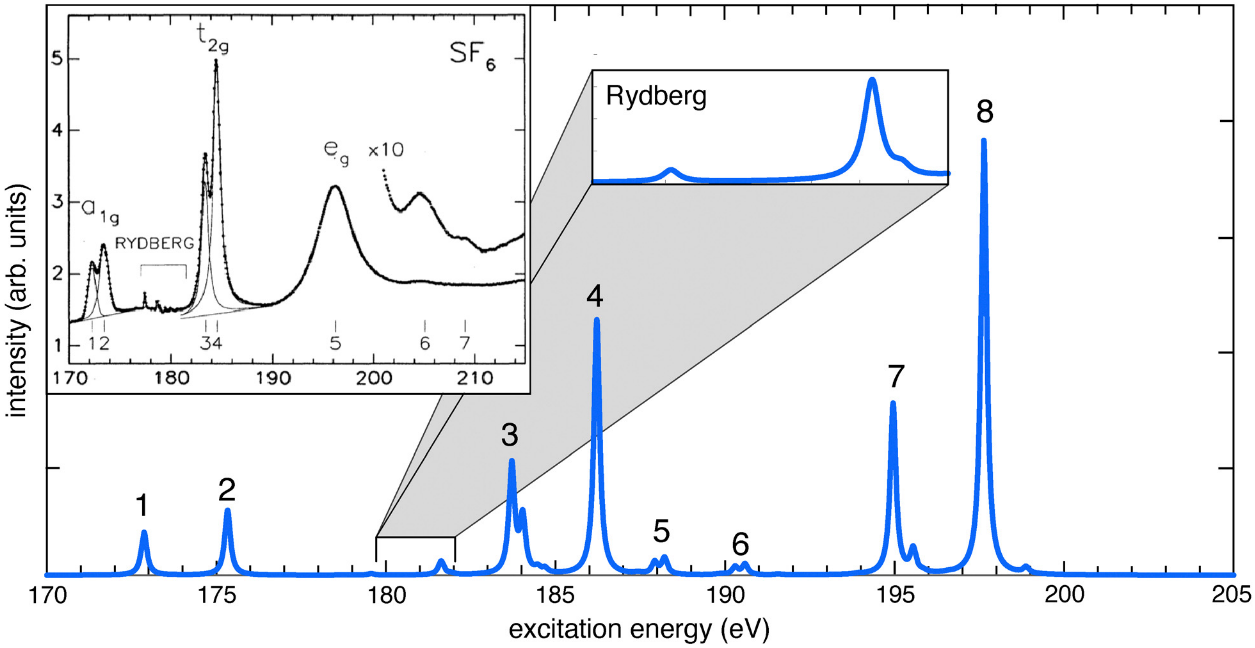

Fig. 7 L-edge XAS of SF_6. The CAM-B3LYP/CIS + SOC spectrum (in blue) was obtained using the def2-TZVPD basis set with 200 singlet and 200 triplet states. Individual transition energies were shifted by 5 eV and broadened with a Lorentzian function (FWHM = 0.3 eV). The experimental spectrum (inset) is reproduced from ref. 134; copyright 1993 American Physical Society.

co-workers have identified the same Rydberg features in real-time TD-DFT calculations,[46] which are found to be quite sensitive to basis-set effects. Since these features are not as important in the context of using L-edge spectroscopy to probe valence virtual orbitals, they are not discussed any further.

The DFT/CIS spectrum for SF_6 in Fig. 7 shows doublet peak structure in all features, with an average splitting of ≈ 2.5 eV as compared to experimental splittings of ≈ 1.2 eV. Nominally, the intensity ratio ratio of the $2p_{3/2}$ to $2p_{1/2}$ features should be about 2 : 1 for each pair of peaks, corresponding to the 4 : 2 ratio of microstates. However, both experimental and ligand-field multiplet intensity ratios can deviate from this result in practice,[124,135] and in the present example this ratio is inverted. The calculated (CAM-B3LYP/CIS + SOC) intensity ratio is 1 : 1.5 for the a_{1g} features (peaks 1 and 2 in Fig. 7), as compared to an experimental ratio of 1 : 1.6. For the t_{2g} features (peaks 3 and 4), the calculations afford an intensity ratio of 1 : 2.24 as compared to an experimental ratio of 1 : 2.04. Previous work indicates that a significant exchange interaction between the core-excited electron and the valence electrons is responsible for this inversion in the $2p_{3/2} : 2p_{1/2}$ intensity ratio.[134]

4.4.2 3d^0 complexes. Core-level spectra of tetrahedrally coordinated 3d^0 metal oxide anions MO_4^{n-} (M = Ti, V, Cr, Mn) are examined in Fig. 8. The 2p → 3d transition is dipole-allowed and the peak splitting affords insight into the electronic structure of the metal 3d band and the effect of the ligand field. The d^0 nature of the ground state means that each ion has only one reasonable ground-state electron configuration, thus a single-reference method like DFT/CIS may be adequate.

Spectra at the metal $L_{2,3}$ edge are shown in Fig. 8a and b. The most apparent feature is the magnitude of the spin–orbit splitting between the L_3 and L_2 edges, which decreases in the order $MnO_4^{-} > CrO_4^{2-} > VO_4^{3-} > TiO_4^{4-}$ in both CAM-B3LYP/CIS + SOC simulations and experiment. The splitting between experimental features labeled A and B (Fig. 8b) decreases in the same order. A similar trend is observed at the oxygen K-edge; see Fig. 8c. The biggest discrepancy between theory and experiment is an inversion of peak intensities between the L_2 and L_3 edges, as observed in previous calculations.[123,124] This is similar to what we observed for $TiCl_4$ (Fig. 1), where it appears that a variational description of SOC is required in order to obtain the correct relative intensities, as discussed in Section 4.1.

SOC increases with atomic number [eqn (11)] and this is reflected in both theory and experiment. However, these MO_4^{n-} spectra exhibit ligand-field splitting (into e and t_{2g} orbitals) at both the L_3 and L_2 edges,[131] such that there are two sets of metal d orbitals available to a 3d^0 transition metal. Oxygen K-edge spectra of these MO_4^{n-} complexes show a splitting in their most intense features that correlates well with the $L_{2,3}$ splitting,[131] indicating that the transition from O(1s) either the e or t_{2g} orbitals is dipole-allowed. Brydson *et al.*[131] argue that there is considerable mixing between the O(2p) and M(3d) orbitals, along with some contribution from M(4p) and O(2s) orbitals, resulting in the nominal O(1s) → M(3d) transition becoming dipole-allowed. The increased splitting between the A and B features at the metal L_3 edge has been attributed to the increasing X–O bond lengths and decreasing formal charge on the metal ion.[131]

4.4.3 Ligand effects at the Fe L-edge. Sensitivity of transition metal 3d orbital energies to ligand substitution is especially pronounced for $Fe(CO)_5$ and $Fe(Cp)_2$ (ferrocene),[130,136] where "Cp" indicates the cyclopentadienyl anion, $(C_5H_6)^-$. $L_{2,3}$-edge spectra of $Fe(CO)_5$ exhibit a splitting in both the L_3 and L_2

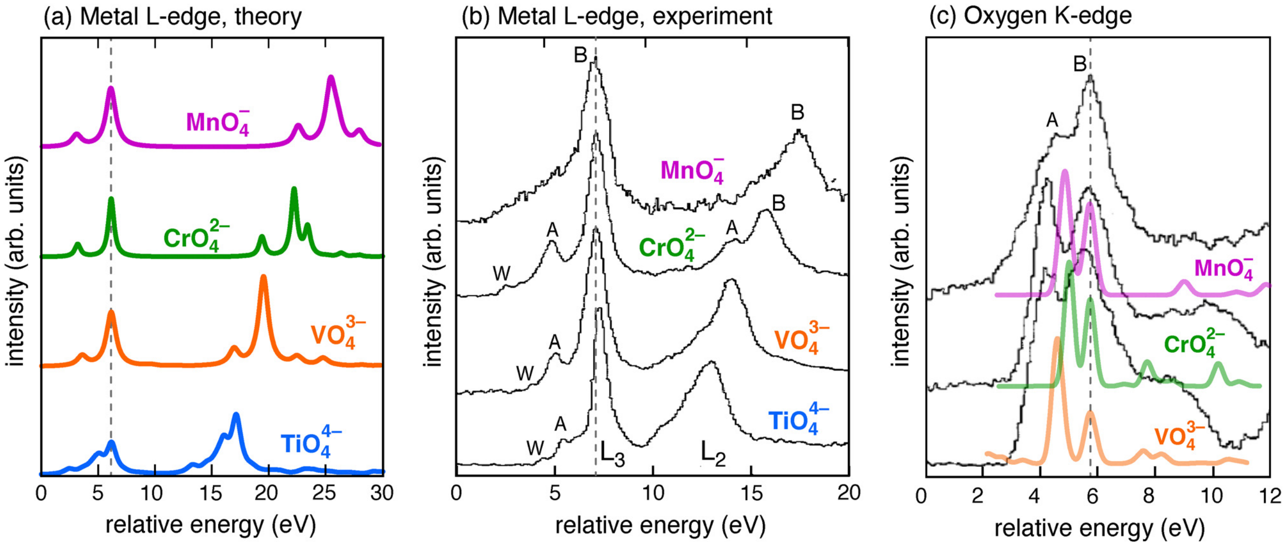

Fig. 8 XAS of 3d^0 metal oxide ions, MO_4^{n-}, including (a) spectra at the metal L-edge from CAM-B3LYP/CIS + SOC calculations, (b) the corresponding experimental L-edge spectra, and (c) oxygen K-edge spectra, overlaying theory (in translucent color) and experiment. Spectra are shifted to align the L_3- or K-edge feature labeled "B", as indicated by the dashed vertical lines. This places all spectra within the same energy window, consistent with the presentation in ref. 131. Simulated spectra were computed using def2-TZPVD including 200 singlet and 200 triplet basis states and broadened using a Lorentzian function (FWHM = 0.3 eV). Experimental spectra are reproduced from ref. 131.

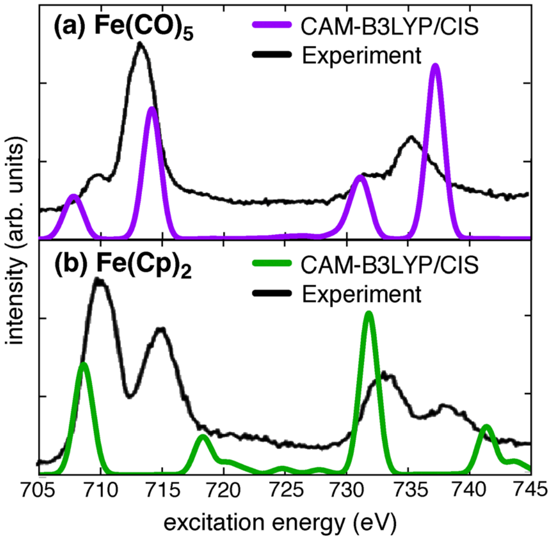

Fig. 9 $L_{2,3}$-edge spectra of (a) $Fe(CO)_5$ and (b) $Fe(Cp)_2$, comparing experiment (with an offset baseline) to CAM-B3LYP/CIS + SOC simulations. The calculations employ the def2-TZVPD basis set with 200 singlet and 200 triplet states, broadened using a Lorentzian function (FWHM = 0.7 eV). The computed spectra are were shifted by (a) 8.0 eV and (b) 10.0 eV in order to align with experimental spectra that are reproduced from ref. 130.

bands, with one peak that is much stronger than the other. This is characteristic of the metal 2p spectra of all near-covalent complexes.[137] In Fig. 9a, we see that this feature is present in both the experimental spectra of $Fe(CO)_5$ and in CAM-B3LYP/CIS + SOC simulations.

The $L_{2,3}$-edge spectrum of ferrocene show significant differences as compared to the iron pentacarbonyl complex, and these differences are reflected in the calculations. This highlights L-edge sensitivity to metal oxidation state and ligand identity. In $Fe(Cp)_2$, the more intense first peak at 709 eV is a $Fe(2p) \rightarrow e_{1g}$ transition, as determined in previous calculations.[137] The second peak has been attributed to a $Fe(2p) \rightarrow e_{2u}$ transition where the $3e_{2u}$ MO contains a significant contribution from Fe(3d) orbitals, giving it metal-to-ligand charge-transfer character.[137]

CAM-B3LYP/CIS + SOC calculations predict a larger $L_{2,3}$ splitting for $Fe(Cp)_2$ as compared to what is observed experimentally. This might be due to the presence of large amounts of exact exchange in the CAM-B3LYP/CIS method, which is known to adversely affect the splitting between high- and low-spin configurations of 3d transition metals.[138–141] Specifically in the context of L-edge spectroscopy, Kasper *et al.*[122] observe larger d-orbital splittings when the half-and-half functional BH&HLYP is used, as compared to B3LYP or PBE0. Indeed, ligand-field splittings often vary directly with the fraction of exact exchange,[142] and functionals with larger fractions (even 20%) tend to overestimate the d-orbital splitting.[138] Overall, the CAM-B3LYP/CIS + SOC approach replicates experimental features and ligand effects with reasonable accuracy, however. This is important for L-edge X-ray spectroscopy where changes in the coordination environment around a metal center are directly observable in experimental spectra.

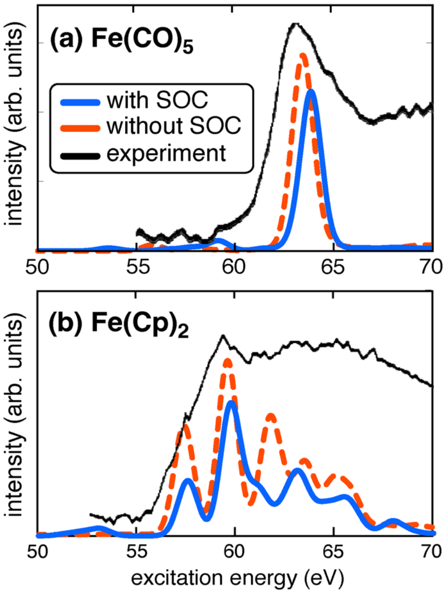

Fig. 10 XUV spectra of (a) $Fe(CO)_5$ and (b) $Fe(Cp)_2$ at the Fe M-edge, comparing CAM-B3LYP/CIS simulations to experimental spectra from ref. 130. Calculations employ the def2-TZVPD basis set with 200 singlet and 200 triplet states. Transition energies were broadened using a Lorentzian function (FWHM = 0.5 eV) but have not been shifted.

4.5 M-edge spectra

Finally, we consider $M_{2,3}$-edge spectra of some 3d transition metal complexes. Fig. 10 presents M-edge spectra of the same two iron complexes whose L-edge spectra were discussed in Section 4.4.3, namely, $Fe(CO)_5$ and $Fe(Cp)_2$.[130] The M-edge spectrum of TiO_2 is plotted in Fig. 11, from a thin film of the rutile polymorph,[143,144] and juxtaposed with a CAM-B3LYP/CIS spectrum of its fundamental octahedral unit, $(TiO_6)^{8-}$.

Unlike the L-edge spectra, no shifts are needed to match with experiment in any of these M-edge cases, demonstrating that errors due to SIE are reduced for orbitals with principal quantum number $n = 3$ (M-edge), as compared to those with $n = 2$ (L-edge). Furthermore, SOC effects are no longer

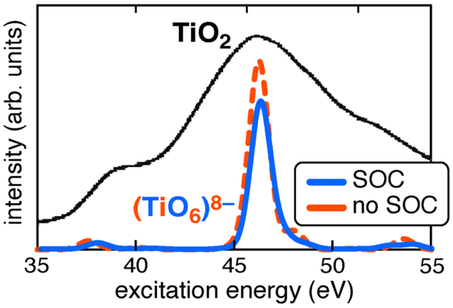

Fig. 11 XUV spectra at the Ti M-edge, for a rutile TiO_2 film (experiment) and its fundamental octahedral unit $(TiO_6)^{8-}$ (CAM-B3LYP/CIS calculation). The experimental spectrum is reproduced from ref. 144 but was originally recorded in ref. 143. Calculations use the def2-TZVPD basis set and include 200 singlet and 200 triplet states, with transition energies that are broadened using a Lorentzian function (FWHM = 0.5 eV) but not shifted.

significant and similar spectral features are obtained using nonrelativistic calculations. This is consistent with the larger electron–nucleus separation for the 3p orbitals and the r^{-3} distance dependence of SOC [eqn (11) and (12)]. With or without SOC, the CAM-B3LYP/CIS spectra resemble the experimental ones, including the abrupt M-edge in $Fe(CO)_5$, the broad multiplet in $Fe(Cp)_2$, and a low-energy shoulder in TiO_2. The spin–orbit splitting is much reduced even as compared to the same Fe complexes at the L-edge (*cf.* Fig. 9).

5 Conclusions

This work extends a new CAM-B3LYP/CIS variant[55] of the DFT/CIS method[56] to core-level spectroscopy at elemental L- and M-edges. Specifically, a state-interaction treatment of SOC, using the Breit–Pauli Hamiltonian within a mean-field approximation for the matrix elements, is used to correct the nonrelativistic (SOC-free) DFT/CIS states. The same approach works for TD-DFT calculations as well,[95] but CAM-B3LYP/CIS was parameterized in such a way that it significantly reduces the *ad hoc* shifts that are necessary to match experiment for core-to-valence excitation energies. Although these shifts were parameterized at elemental K-edges,[55] we find that the same parameterization also yields more accurate results for L- and M-edge spectra, as compared to TD-DFT with general-purpose functionals.

The cost of the DFT/CIS calculations is the same as that of CIS calculations and, when combined with the CVS approximation, is significantly cheaper than the real-time TD-DFT approach.[35] SOC corrections implemented in the Q-Chem program[105] can be added to nonrelativistic DFT/CIS and TD-DFT calculations *a posteriori*, using a Python package developed for this work.[106]

The CAM-B3LYP/CIS + SOC method accurately models L- and M-edge spectra, as assessed herein by comparison to experimental results. The CVS approximation, which reduces the active space to a small number of occupied orbitals appropriate for the elemental edge in question, significantly reduces the cost although a large number of excited states is required to converge spectral lineshapes. The CVS approximation is also vital for disentangling overlapping spectral features and making peak assignments. At present, the SOC corrections are implemented only for closed-shell species and we hope to introduce an open-shell variant in due course, enabling simulations of core-level spectra on a wider range of transition metal systems.

Author contributions

Aniket Mandal: conceptualization (contributing); data curation (lead); formal analysis (lead); investigation (lead); methodology (lead); software (lead); validation (lead); visualization (lead); writing – original draft (lead); writing – review and editing (equal). John M. Herbert: conceptualization (lead); formal analysis (contributing); funding acquisition (lead); methodology (contributing); project administration (lead); supervision (lead); visualization (contributing); writing – review and editing (equal).

Conflicts of interest

J. M. H. is part owner of Q-Chem Inc. and serves on its board of directors.

Data availability

The data that support these findings are available from the corresponding author upon reasonable request.

Acknowledgements

Work by A. M. to develop DFT/CIS was supported by the donors of American Chemical Society Petroleum Research Fund (grant no. 62041-ND6) while work to implement SOC was supported by the National Science Foundation (grant numbers CHE-1955282 and CHE-2402361). Calculations were performed at the Ohio Supercomputer Center.[145]

References

1 F. M. F. de Groot, M. Grioni, J. C. Fuggle, J. Ghijsen, G. A. Sawatzky and H. Petersen, Oxygen 1s X-ray-absorption edges of transition-metal oxides, *Phys. Rev. B:Condens. Matter Mater. Phys.*, 1989, **40**, 5715–5723.
2 F. M. F. de Groot, XANES spectra of transition metal compounds, *J. Phys.:Conf. Ser.*, 2009, **190**, 012004.
3 S. I. Bokarev and O. Kühn, Theoretical X-ray spectroscopy of transition metal compounds, *Wiley Interdiscip. Rev.:Comput. Mol. Sci.*, 2020, **10**, e1433.
4 T. M. Willey, J. R. I. Lee, D. Brehmer, O. A. P. Mellone, L. Landt, P. R. Schreiner, A. A. Fokin, B. A. Tkachenko, A. de Meijere, S. Kozhushkov and A. W. van Buuren, X-ray spectroscopic identification of strain and structure-based resonances in a series of saturated carbon-cage molecules: Adamantane, twistane, octahedrane, and cubane, *J. Vac. Sci. Technol., A*, 2021, **39**, 053208.
5 S. Adak, M. Hartl, L. Daemen, E. Fohtung and H. Nakotte, Study of oxidation states of the transition metals in a series of Prussian blue analogs using X-ray absorption near edge structure (XANES) spectroscopy, *J. Electron Spectrosc. Relat. Phenom.*, 2017, **214**, 8–19.
6 M. Lundberg and M. G. Delcey, Multiconfigurational approach to X-ray spectroscopy of transition metal compounds, in *Transition Metals in Coordination Environments*, ed. E. Broclawik, T. Borowski, and M. Radoń, Springer Nature, Switzerland, 2019, vol. 29 of Challenges and Advances in Computational Chemistry and Physics, pp. 185–217.
7 K. Stanistreet-Welsh and A. Kerridge, Bounding $[AnO_2]^{2+}$ (An = U, Np) covalency by simulated O K-edge and An

M-edge X-ray absorption near-edge spectroscopy, *Phys. Chem. Chem. Phys.*, 2023, 25, 23753–23760.

8 M. L. Baker, M. W. Mara, J. J. Yan, K. O. Hodgson, B. Hedman and E. I. Solomon, K- and L-edge X-ray absorption spectroscopy (XAS) and resonant inelastic X-ray scattering (RIXS) determination of differential orbital covalency (DOC) of transition metal sites, *Coord. Chem. Rev.*, 2017, **345**, 182–208.

9 G. Kaindl, G. Kalkowski, W. D. Brewer, B. Perscheid and F. Holtzberg, M-edge X-ray absorption spectroscopy of 4f instabilities in rare-earth systems (invited), *J. Appl. Phys.*, 1984, **55**, 1910–1915.

10 F. de Groot and A. Kotani, *Core Level Spectroscopy of Solids*, CRC Press, Boca Raton, 2008.

11 H. Wang, A. T. Young, J. Guo, S. P. Cramer, S. Friedrich, A. Braun and W. Gu, Soft X-ray absorption spectroscopy and resonant inelastic X-ray scattering spectroscopy below 100 eV: Probing first-row transition-metal M-edges in chemical complexes, *J. Synchrotron Radiat.*, 2013, **20**, 614–619.

12 W. Gu, H. Wang and K. Wang, Nickel L-edge and K-edge X-ray absorption spectroscopy of non-innocent $Ni[S_2C_2(CF_3)_2]_2^n$ series (n = −2, −1, 0): Direct probe of nickel fractional oxidation state changes, *Dalton Trans.*, 2014, **43**, 6406–6413.

13 J. Vura-Weis, C.-M. Jiang, C. Liu, H. Gao, J. M. Lucas, F. M. F. de Groot, P. Yang, A. P. Alivasatos and S. R. Leone, Femtosecond $M_{2,3}$-edge spectroscopy of transition metal oxides: Photoinduced oxidation state change in α-Fe_2 O_3, *J. Phys. Chem. Lett.*, 2013, **4**, 3667–3671.

14 C.-M. Jiang, L. R. Baker, J. M. Lucas, J. Vura-Weis, A. P. Alivisatos and S. R. Leone, Characterization of photo-induced charge transfer and hot carrier relaxation pathways in spinel cobalt oxide (Co_3O_4), *J. Phys. Chem. C*, 2014, **118**, 22774–22784.

15 C. A. Leahy and J. Vura-Weis, Femtosecond extreme ultraviolet spectroscopy of an iridium photocatalyst reveals oxidation state and ligand field specific dynamics, *J. Phys. Chem. A*, 2022, **126**, 9510–9518.

16 L. R. Baker, C.-M. Jiang, S. T. Kelly, J. M. Lucas, J. Vura-Weis, M. K. Gilles, A. P. Alivisatos and S. R. Leone, Charge carrier dynamics of photoexcited Co_3O_4 in methanol: Extending high harmonic transient absorption spectroscopy to liquid environments, *Nano Lett.*, 2014, **14**, 5883–5890.

17 M. Kubin, M. Guo, T. Kroll, H. Löchel, E. Källman, M. L. Baker, R. Mitzner, S. Gul, J. Kern, A. Föhlisch, A. Erko, U. Bergmann, V. Yachandra, J. Yano, M. Lundberg and P. Wernet, Probing the oxidation state of transition metal complexes: A case study on how charge and spin densities determine Mn L-edge X-ray absorption energies, *Chem. Sci.*, 2018, **9**, 6813–6829.

18 F. M. F. de Groot, Z. W. Hu, M. F. Lopez, G. Kaindl, F. Guillot and M. Tronc, Differences between L_3 and L_2 X-ray absorption spectra of transition metal compounds, *J. Chem. Phys.*, 1994, **101**, 6570–6576.

19 J. N. Ehrman, K. Shumilov, A. J. Jenkins, J. M. Kasper, T. Vitova, E. R. Batista, P. Yang and X. Li, Unveiling hidden shake-up features in the uranyl M_4-edge spectrum, *J. Am. Chem. Soc. Au*, 2024, **4**, 1134–1141.

20 G. Cressey, C. M. B. Henderson and G. van der Laan, Use of *L*-edge X-ray absorption spectroscopy to characterize multiple valence states of 3d transition metals; a new probe for mineralogical and geochemical research, *Phys. Chem. Miner.*, 1993, **20**, 111–119.

21 J. T. Lau, K. Hirsch, P. Klar, A. Langenberg, F. Lofink, R. Richter, J. Rittmann, M. Vogel, V. Zamudio-Bayer, T. Möller and B. V. Issendorff, X-ray spectroscopy reveals high symmetry and electronic shell structure of transition-metal-doped silicon clusters, *Phys. Rev. A:At., Mol., Opt. Phys.*, 2009, **79**, 053201.

22 G. Lucovsky, L. Miotti, D. Zeller, C. Adamo and D. Scholm, X-ray absorption studies of elemental and complex transition metal (TM) oxides: Differences between: (i) chemical, and (ii) local site symmetry multivalency, in *Ulis 2011 Ultimate Integration on Silicon*, 2011, pp. 1–4.

23 T. Hayakawa, K. Egashira, M. Arakawa, T. Ito, S. Sarugaku, K. Ando and A. Terasaki, X-ray absorption spectroscopy of $Ce2O_3^+$ and $Ce_2O_5^+$ near Ce M-edge, *J. Phys. B:At., Mol. Opt. Phys.*, 2016, **49**, 075101.

24 J. Lüder, J. Schött, B. Brena, M. W. Haverkort, P. Thunström, O. Eriksson, B. Sanyal, I. Di Marco and Y. O. Kvashnin, Theory of *L*-edge spectroscopy of strongly correlated systems, *Phys. Rev. B*, 2017, **96**, 245131.

25 F. de Groot, Multiplet effects in X-ray spectroscopy, *Coord. Chem. Rev.*, 2005, **249**, 31–63.

26 M. W. Haverkort, M. Zwierzycki and O. K. Andersen, Multiplet ligand-field theory using Wannier orbitals, *Phys. Rev. B:Condens. Matter Mater. Phys.*, 2012, **85**, 165113.

27 F. M. F. de Groot, H. Elnaggar, F. Frati, R. Wang, M. U. D. M. van Veenendaal, J. Fernandez-Rodriguez, M. W. Haverkort, R. J. Green, G. van der Laan, Y. Kvashnin, A. Hariki, H. Ikeno, H. Ramanantoanina, C. Daul, B. Delley, M. Odelius, M. Lundberg, O. Kuhn, S. I. Bokarev, E. Shirley, J. Vinson, K. Gilmore, M. Stener, G. Fronzoni, P. Decleva, P. Kruger, M. Retegan, Y. Joly, C. Vorwerk, C. Draxl, J. Rehr and A. Tanaka, 2p X-ray absorption spectroscopy of 3d transition metal systems, *J. Electron Spectrosc. Relat. Phenom.*, 2021, **249**, 147061.

28 I. Josefsson, K. Kunnus, S. Schreck, A. Föhlisch, F. de Groot, P. Wernet and M. Odelius, Ab initio calculations of X-ray spectra: Atomic multiplet and molecular orbital effects in a multiconfigurational SCF approach to the L-edge spectra of transition metal complexes, *J. Phys. Chem. Lett.*, 2012, **3**, 3565–3570.

29 A. Chantzis, J. K. Kowalska, D. Maganas, S. DeBeer and F. Neese, *Ab initio* wave function-based determination of element specific shifts for the efficient calculation of X-ray absorption spectra of main group elements and first row transition metals, *J. Chem. Theory Comput.*, 2018, **14**, 3686–3702.

30 P. Norman and A. Dreuw, Simulating X-ray spectroscopies and calculating core-excited states of molecules, *Chem. Rev.*, 2018, **118**, 7208–7248.

31 I. Seidu, S. P. Neville, M. Kleinschmidt, A. Heil, C. M. Marian and M. S. Schuurman, The simulation of X-ray absorption spectra from ground and excited electronic states using core-valence separated DFT/MRCI, *J. Chem. Phys.*, 2019, **151**, 144104.

32 M. L. Vidal, P. Pokhilko, A. I. Krylov and S. Coriani, Equation-of-motion coupled-cluster theory to model L-edge X-ray absorption and photoelectron spectroscopy, *J. Phys. Chem. Lett.*, 2020, **11**, 8314–8321.

33 N. A. Besley, Density functional theory based methods for the calculation of X-ray spectroscopy, *Acc. Chem. Res.*, 2020, **53**, 1306–1315.

34 N. A. Besley, Modeling of the spectroscopy of core electrons with density functional theory, *Wiley Interdiscip. Rev.:Comput. Mol. Sci.*, 2021, **12**, e1527.

35 J. M. Herbert, Y. Zhu, B. Alam and A. K. Ojha, Time-dependent density functional theory for X-ray absorption spectra: Comparing the real-time approach to linear response, *J. Chem. Theory Comput.*, 2023, **19**, 6745–6760.

36 D. R. Nascimento and N. Govind, Computational approaches for XANES, VtC-XES, and RIXS using linear-response time-dependent density functional theory based methods, *Phys. Chem. Chem. Phys.*, 2022, **24**, 14680–14691.

37 J. M. Herbert, Density-functional theory for electronic excited states, in *Theoretical and Computational Photochemistry: Fundamentals, Methods, Applications and Synergy with Experimental Approaches*, ed. C. García-Iriepa and M. Marazzi, Elsevier, Amsterdam, 2023, ch. 3, pp. 69–118.

38 T. Fransson, I. E. Brumboiu, M. L. Vidal, P. Norman, S. Coriani and A. Dreuw, XABOOM: An X-ray absorption benchmark of organic molecules based on carbon, nitrogen, and oxygen 1s → π* transitions, *J. Chem. Theory Comput.*, 2021, **17**, 1618–1637.

39 L. Konecny, J. Vicha, S. Komorovsky, K. Ruud and M. Repisky, Accurate X-ray absorption spectra near L- and M-edges from relativistic four-component damped response time-dependent density functional theory, *Inorg. Chem.*, 2021, **61**, 830–846.

40 Y. Imamura and H. Nakai, Analysis of self-interaction correction for describing core excited states, *Int. J. Quantum Chem.*, 2007, **107**, 23–29.

41 Y. Imamura, T. Otsuka and H. Nakai, Description of core excitations by time-dependent density functional theory with local density approximation, generalized gradient approximation, meta-generalized gradient approximation, and hybrid functionals, *J. Comput. Chem.*, 2007, **28**, 2067–2074.

42 Y. Imamura and H. Nakai, Description of core-ionized and core-excited states by density functional theory and time-dependent density functional theory, in *Quantum Systems in Chemistry and Physics*, ed. K. Nishikawa, J. Maruani, E. J. Brändas, G. Delgado-Barrio and P. Piecuch, Spring Science + Business Media, Dordrecht, 2012, vol. 26 of Progress in Theoretical Chemistry and Physics, ch. 14, pp. 275–308.

43 N. A. Besley, M. J. G. Peach and D. J. Tozer, Time-dependent density functional theory calculations of near-edge X-ray absorption fine structure with short-range corrected functionals, *Phys. Chem. Chem. Phys.*, 2009, **11**, 10350–10358.

44 J. D. Wadey and N. A. Besley, Quantum chemical calculations of X-ray emission spectroscopy, *J. Chem. Theory Comput.*, 2014, **10**, 4557–4564.

45 I. P. E. Roper and N. A. Besley, The effect of basis set and exchange-correlation functional on the time-dependent density functional theory calculations within the Tamm-Dancoff approximation of the X-ray emission spectroscopy of transition metal complexes, *J. Chem. Phys.*, 2016, **144**, 114104.

46 M. Kadek, L. Konecny, B. Gao, M. Repisky and K. Ruud, X-ray absorption resonances near $L_{2,3}$-edges from real-time propagation of the Dirac-Kohn-Sham density matrix, *Phys. Chem. Chem. Phys.*, 2015, **17**, 22566–22570.

47 R. G. Fernando, M. C. Balhoff and K. Lopata, X-ray absorption in insulators with non-Hermitian real-time time-dependent density functional theory, *J. Chem. Theory Comput.*, 2015, **11**, 646–654.

48 M. Yang, A. Sissay, M. Chen and K. Lopata, Intruder peak-free transient inner-shell spectra using real-time simulations, *J. Chem. Theory Comput.*, 2022, **18**, 992–1002.

49 A. Nakata, Y. Imamura, T. Otsuka and H. Nakai, Time-dependent density functional theory calculations for core-excited states: Assessment of standard exchange-correlation functionals and development of a novel hybrid functional, *J. Chem. Phys.*, 2006, **124**, 094105.

50 A. Nakata, Y. Imamura and H. Nakai, Hybrid exchange-correlation functional for core, valence, and Rydberg excitations: Core-valence-Rydberg B3LYP, *J. Chem. Phys.*, 2006, **125**, 064109.

51 A. Nakata, Y. Imamura and H. Nakai, Extension of the core-valence-Rydberg B3LYP functional to core-excited-state calculations of third-row atoms, *J. Chem. Theory Comput.*, 2007, **3**, 1295–1305.

52 N. A. Besley and F. A. Asmuruf, Time-dependent density functional theory calculations of the spectroscopy of core electrons, *Phys. Chem. Chem. Phys.*, 2010, **12**, 12024–12039.

53 D. Hait, K. J. Oosterbaan, K. Carter-Fenk and M. Head-Gordon, Computing X-ray absorption spectra from linear-response particles atop optimized holes, *J. Chem. Phys.*, 2022, **156**, 201104.

54 K. Carter-Fenk, L. A. Cunha, J. E. Arias-Martinez and M. Head-Gordon, Electron-affinity time-dependent density functional theory: Formalism and applications to core-excited states, *J. Phys. Chem. Lett.*, 2022, **13**, 9664–9672.

55 A. Mandal, E. J. Berquist and J. M. Herbert, A new parameterization of the DFT/CIS method with applications to core-level spectroscopy, *J. Chem. Phys.*, 2024, **161**, 044114.

56 S. Grimme, Density functional calculations with configuration interaction for the excited states of molecules, *Chem. Phys. Lett.*, 1996, **259**, 128–137.

57 A. Stolow, Femtosecond time-resolved photoelectron spectroscopy of polyatomic molecules, *Annu. Rev. Phys. Chem.*, 2003, **54**, 89–119.

58 P. Glatzel and U. Bergmann, High resolution 1s core hole X-ray spectroscopy in 3d transition metal complexes--electronic and structural information, *Coord. Chem. Rev.*, 2005, **249**, 65–95.

59 T. Yamamoto, Assignment of pre-edge peaks in K-edge X-ray absorption spectra of 3d transition metal compounds: Electric dipole or quadrupole?, *X-Ray Spectrom.*, 2008, **37**, 572–584.

60 F. de Groot, G. Vankó and P. Glatzel, The 1s X-ray absorption pre-edge structures in transition metal oxides, *J. Phys.:Condens. Matter*, 2009, **21**, 104207.

61 K. Zhang, M.-F. Lin, E. S. Ryland, M. A. Verkamp, K. Benke, F. M. F. de Groot, G. S. Girolami and J. Vura-Weis, Shrinking the synchrotron: Tabletop extreme ultraviolet absorption of transition-metal complexes, *J. Phys. Chem. Lett.*, 2016, **7**, 3383–3387.

62 E. S. Ryland, M.-F. Lin, M. A. Verkamp, K. Zhang, K. Benke, M. Carlson and J. Vura-Weis, Tabletop femtosecond M-edge X-ray absorption near-edge structure of FeTPPCI: Metalloporphyrin photophysics from the perspective of the metal, *J. Am. Chem. Soc.*, 2018, **140**, 4691–4696.

63 K. Zhang, R. Ash, G. S. Girolami and J. Vura-Weis, Tracking the metal-centered triplet in photoinduced spin crossover of $Fe(phen)_3{}^{2+}$ with tabletop femtosecond M-edge X-ray absorption near-edge structure spectroscopy, *J. Am. Chem. Soc.*, 2019, **141**, 17180–17188.

64 A. S. Chatterley, F. Lackner, C. D. Pemmaraju, D. M. Neumark, S. R. Leone and O. Gessner, Dissociation dynamics and electronic structures of highly excited ferrocenium ions studied by femtosecond XUV absorption spectroscopy, *J. Phys. Chem. A*, 2016, **120**, 9509–9518.

65 A. Cirri, J. Husek, S. Biswas and L. R. Baker, Achieving surface sensitivity in ultrafast XUV spectroscopy: $M_{2,3}$-edge reflection-absorption of transition metal oxides, *J. Phys. Chem. C*, 2017, **121**, 15861–15869.

66 J. Husek, A. Cirri, S. Biswas and L. R. Baker, Surface electron dynamics in hematite (α-Fe_2O_3): Correlation between ultrafast surface electron trapping and small polaron formation, *Chem. Sci.*, 2017, **8**, 8170–8178.

67 S. Biswas, J. Husek and L. R. Baker, Elucidating ultrafast electron dynamics at surfaces using extreme ultraviolet (XUV) reflection-absorption spectroscopy, *Chem. Commun.*, 2018, **54**, 4216–4230.

68 S. Biswas, J. Husek, S. Londo and L. R. Baker, Ultrafast electron trapping and defect-mediated recombination in NiO probed by femtosecond extreme ultraviolet reflection-absorption spectroscopy, *J. Phys. Chem. Lett.*, 2018, **9**, 5047–5054.

69 J. Vura-Weis, Femtosecond extreme ultraviolet absorption spectroscopy of transition metal complexes, *Annu. Rev. Phys. Chem.*, 2025, **76**, 455–470.

70 J. M. Kasper, T. F. Stetina, A. J. Jenkins and X. Li, *Ab initio* methods for L-edge X-ray absorption spectroscopy, *Chem. Phys. Rev.*, 2020, **1**, 011304.

71 A. Dreuw and M. Head-Gordon, Single-reference ab initio methods for the calculation of excited states of large molecules, *Chem. Rev.*, 2005, **105**, 4009–4037.

72 T. Yanai, D. P. Tew and N. C. Handy, A new hybrid exchange-correlation functional using the Coulomb-attenuating method (CAM-B3LYP), *Chem. Phys. Lett.*, 2004, **393**, 51–57.

73 R. Kobayashi and R. D. Amos, The application of CAM-B3LYP to the charge-transfer band problem of the zincbateriochlorin-bacteriochlorin complex, *Chem. Phys. Lett.*, 2006, **420**, 106–109.

74 Z.-L. Cai, M. J. Crossley, J. R. Reimers, R. Kobayashi and R. D. Amos, Density functional theory for charge transfer: The nature of the N-bands of porphyrins and chlorophylls revealed through CAM-B3LYP, CASPT2, and SAC-CI calculations, *J. Phys. Chem. B*, 2006, **110**, 15624–15632.

75 M. J. G. Peach, P. Benfield, T. Helgaker and D. J. Tozer, Excitation energies in density functional theory: An evaluation and a diagnostic test, *J. Chem. Phys.*, 2008, **128**, 044118.

76 B. Alam, A. F. Morrison and J. M. Herbert, Charge separation and charge transfer in the low-lying excited states of pentacene, *J. Phys. Chem. C*, 2020, **124**, 24653–24666.

77 D. Rappoport and F. Furche, Property-optimized Gaussian basis sets for molecular response calculations, *J. Chem. Phys.*, 2010, **133**, 134105.

78 S. Pak and D. R. Nascimento, The role of the coupling matrix elements in time-dependent density functional theory on the simulation of core-level spectra of transition metal complexes, *Electron. Struct.*, 2024, **6**, 015014.

79 P.-F. Loos, A. Scemama, A. Blondel, Y. Garniron, M. Caffarel and D. Jacquemin, A mountaineering strategy to excited states: Highly accurate reference energies and benchmarks, *J. Chem. Theory Comput.*, 2018, **14**, 4360–4379.

80 T. Saue, Relativistic Hamiltonians for chemistry: A primer, *ChemPhysChem*, 2011, **12**, 3077–3094.

81 O. Takahashi, Relativistic corrections for single- and double-core excitations at the K- and L-edges from Li to Kr, *Comput. Theor. Chem.*, 2017, **1102**, 80–86.

82 S. Jana and J. M. Herbert, Slater transition methods for core-level electron binding energies, *J. Chem. Phys.*, 2023, **158**, 094111.

83 S. Jana and J. M. Herbert, Fractional-electron and transition-potential methods for core-to-valence excitation energies using density functional theory, *J. Chem. Theory Comput.*, 2023, **19**, 4100–4113.

84 E. van Lenthe, J. G. Snijders and E. J. Baerends, The zero-order regular approximation for relativistic effects: The effect of spin-orbit coupling in closed shell molecules, *J. Chem. Phys.*, 1996, **105**, 6506–6516.

85 M. Douglas and N. M. Kroll, Quantum electrodynamical corrections to the fine structure of helium, *Ann. Phys.*, 1974, **82**, 89–155.

86 I. Miroslav and T. Saue, An infinite-order two-component relativistic Hamiltonian by a simple one-step transformation, *J. Chem. Phys.*, 2007, **126**, 064102.

87 L. Cheng, F. Wang, J. F. Stanton and J. Gauss, Perturbative treatment of spin-orbit-coupling within spin-free exact two-component theory using equation-of-motion coupled-cluster methods, *J. Chem. Phys.*, 2018, **148**, 044108.

88 U. Wahlgren, M. Sjøvoll, H. Fagerli, O. Gropen and B. Schimmelpfennig, *Ab initio* calculation of the $^2P_{1/2}$–$^2P_{3/2}$ splitting in the thallium atom, *Theor. Chem. Acc.*, 1997, **97**, 324–330.

89 Z. Lin, C. Zhang and L. Cheng, Comparison of state-interaction and spinor-representation calculations of spin-orbit coupling within exact two-component coupled-cluster theories, *Mol. Phys.*, 2025, **123**, e2256423.

90 B. A. Heß, C. M. Marian, U. Wahlgren and O. Gropen, A mean-field spin-orbit method applicable to correlated wavefunctions, *Chem. Phys. Lett.*, 1996, **251**, 365–371.

91 C. M. Marian, Spin-orbit coupling and intersystem crossing in molecules, *Wiley Interdiscip. Rev.:Comput. Mol. Sci.*, 2012, **2**, 187–203.

92 E. Epifanovsky, K. Klein, S. Stopkowicz, J. Gauss and A. I. Krylov, Spin-orbit couplings within the equation-of-motion coupled-cluster framework: Theory, implementation, and benchmark calculations, *J. Chem. Phys.*, 2015, **143**, 064102.

93 P. Pokhilko, E. Epifanovsky and A. I. Krylov, General framework for calculating spin-orbit couplings using spinless one-particle density matrices: Theory and application to the equation-of-motion coupled-cluster wave functions, *J. Chem. Phys.*, 2019, **151**, 034106.

94 A. Carreras, H. Jiang, P. Pokhilko, A. I. Krylov, P. M. Zimmerman and D. Casanova, Calculation of spin-orbit couplings using RASCI spinless one-particle density matrices: Theory and applications, *J. Chem. Phys.*, 2020, **153**, 214107.

95 S. Kotaru, P. Pokhilko and A. I. Krylov, Spin-orbit couplings within spin-conserving and spin-flipping time-dependent density functional theory: Implementation and benchmark calculations, *J. Chem. Phys.*, 2022, **157**, 224110.

96 J. M. Herbert, Visualizing and characterizing excited states from time-dependent density functional theory, *Phys. Chem. Chem. Phys.*, 2024, **26**, 3755–3794.

97 X. Zhang and J. M. Herbert, Analytic derivative couplings in time-dependent density functional theory: Quadratic response theory versus pseudo-wavefunction approach, *J. Chem. Phys.*, 2015, **142**, 064109.

98 E. C. Alguire, Q. Ou and J. E. Subotnik, Calculating derivative couplings between time-dependent Hartree-Fock excited states with pseudo-wavefunctions, *J. Phys. Chem. B*, 2015, **119**, 7140–7149.

99 D. R. Nascimento, E. Biasin, B. I. Poulter, M. Khalil, D. Sokaras and N. Govind, Resonant inelastic X-ray scattering calculations of transition metal complexes within a simplified time-dependent density functional theory framework, *J. Chem. Theory Comput.*, 2021, **17**, 3031–3038.

100 X. Zhang and J. M. Herbert, Spin-flip, tensor equation-of-motion configuration interaction with a density-functional correction: A spin-complete method for exploring excited-state potential energy surfaces, *J. Chem. Phys.*, 2015, **143**, 234107.

101 S. G. Chiodo and N. Russo, DFT spin-orbit coupling between singlet and triplet excited states: A case of psoralen compounds, *Chem. Phys. Lett.*, 2010, **490**, 90–96.

102 S. G. Chiodo and M. Leopoldini, MolSOC: A spin-orbit coupling code, *Comput. Phys. Commun.*, 2014, **185**, 676–683.

103 M. Roemelt, D. Maganas, S. DeBeer and F. Neese, A combined DFT and restricted open-shell configuration interaction method including spin-orbit coupling: Application to transition metal L-edge X-ray absorption spectroscopy, *J. Chem. Phys.*, 2013, **138**, 204101.

104 F. Furche, On the density matrix based approach to time-dependent density functional response theory, *J. Chem. Phys.*, 2001, **114**, 5982–5992.

105 E. Epifanovsky, A. T. B. Gilbert, X. Feng, J. Lee, Y. Mao, N. Mardirossian, P. Pokhilko, A. F. White, M. P. Coons, A. L. Dempwolff, Z. Gan, D. Hait, P. R. Horn, L. D. Jacobson, I. Kaliman, J. Kussmann, A. W. Lange, K. U. Lao, D. S. Levine, J. Liu, S. C. McKenzie, A. F. Morrison, K. D. Nanda, F. Plasser, D. R. Rehn, M. L. Vidal, Z.-Q. You, Y. Zhu, B. Alam, B. J. Albrecht, A. Aldossary, E. Alguire, J. H. Andersen, V. Athavale, D. Barton, K. Begam, A. Behn, N. Bellonzi, Y. A. Bernard, E. J. Berquist, H. G. A. Burton, A. Carreras, K. Carter-Fenk, R. Chakraborty, A. D. Chien, K. D. Closser, V. Cofer-Shabica, S. Dasgupta, M. de Wergifosse, J. Deng, M. Diedenhofen, H. Do, S. Ehlert, P.-T. Fang, S. Fatehi, Q. Feng, T. Friedhoff, J. Gayvert, Q. Ge, G. Gidofalvi, M. Goldey, J. Gomes, C. E. González-Espinoza, S. Gulania, A. O. Gunina, M. W. D. Hanson-Heine, P. H. P. Harbach, A. Hauser, M. F. Herbst, M. Hernández Vera, M. Hodecker, Z. C. Holden, S. Houck, X. Huang, K. Hui, B. C. Huynh, M. Ivanov, A. Jász, H. Ji, H. Jiang, B. Kaduk, S. Kähler, K. Khistyaev, J. Kim, G. Kis, P. Klunzinger, Z. Koczor-Benda, J. H. Koh, D. Kosenkov, L. Koulias, T. Kowalczyk, C. M. Krauter, K. Kue, A. Kunitsa, T. Kus, I. Ladjánszki, A. Landau, K. V. Lawler, D. Lefrancois, S. Lehtola, R. R. Li, Y.-P. Li, J. Liang, M. Liebenthal, H.-H. Lin, Y.-S. Lin, F. Liu, K.-Y. Liu, M. Loipersberger, A. Luenser, A. Manjanath, P. Manohar, E. Mansoor, S. F. Manzer, S.-P. Mao, A. V. Marenich, T. Markovich, S. Mason, S. A. Maurer, P. F. McLaughlin, M. F. S. J. Menger, J.-M. Mewes, S. A. Mewes, P. Morgante, J. W. Mullinax, K. J. Oosterbaan, G. Paran, A. C. Paul, S. K. Paul, F. Pavošević, Z. Pei, S. Prager, E. I. Proynov, A. Rák, E. Ramos-Cordoba, B. Rana, A. E. Rask, A. Rettig, R. M. Richard, F. Rob, E. Rossomme, T. Scheele, M. Scheurer, M. Schneider, N. Sergueev, S. M. Sharada, W. Skomorowski, D. W. Small, C. J. Stein, Y.-C. Su, E. J. Sundstrom, Z. Tao, J. Thirman, G. J. Tornai, T. Tsuchimochi, N. M. Tubman, S. P. Veccham, O. Vydrov, J. Wenzel, J. Witte, A. Yamada, K. Yao, S. Yeganeh, S. R. Yost, A. Zech, I. Y. Zhang, X. Zhang, Y. Zhang, D. Zuev, A. Aspuru-Guzik, A. T. Bell, N. A. Besley, K. B. Bravaya, B. R. Brooks, D. Casanova, J.-D. Chai, S. Coriani, C. J. Cramer, G. Cserey, A. E. DePrince III, R. A. DiStasio Jr., A. Dreuw, B. D. Dunietz, T. R. Furlani, W. A. Goddard III, S. Hammes-Schiffer, T. Head-Gordon, W. J. Hehre, C.-P. Hsu, T.-C. Jagau, Y. Jung, A. Klamt, J. Kong, D. S. Lambrecht, W. Liang, N. J. Mayhall, C. W. McCurdy, J. B. Neaton, C. Ochsenfeld, J. A. Parkhill,

R. Peverati, V. A. Rassolov, Y. Shao, L. V. Slipchenko, T. Stauch, R. P. Steele, J. E. Subotnik, A. J. W. Thom, A. Tkatchenko, D. G. Truhlar, T. Van Voorhis, T. A. Wesolowski, K. B. Whaley, H. L. Woodcock III, P. M. Zimmerman, S. Faraji, P. M. W. Gill, M. Head-Gordon, J. M. Herbert and A. I. Krylov, Software for the frontiers of quantum chemistry: An overview of developments in the Q-Chem 5 package, *J. Chem. Phys.*, 2021, **155**, 084801.

106 pySETSOC, a Q-Chem post-processing program for single-excitation theories with spin–orbit coupling, https://gitlab.com/john-herbert-group/pysetsoc.

107 D. Casanova, Efficient implementation of restricted active space configuration interaction with the hole and particle approximation, *J. Comput. Chem.*, 2012, **34**, 720–730.

108 K. C. Prince, M. Vondráček, J. Karvonen, M. Coreno, R. Camilloni, L. Avaldi and M. de Simone, A critical comparison of selected 1s and 2p core hole widths, *J. Electron Spectrosc. Relat. Phenom.*, 1999, **101–103**, 141–147.

109 C. Nicolas and C. Miron, Lifetime broadening of core-excited and -ionized states, *J. Electron Spectrosc. Relat. Phenom.*, 2012, **185**, 267–272.

110 M. F. Herbst and T. Fransson, Quantifying the error of the core-valence separation approximation, *J. Chem. Phys.*, 2020, **153**, 054114.

111 T. Fransson and L. G. M. Pettersson, Evaluating the impact of the Tamm-Dancoff approximation on X-ray spectrum calculations, *J. Chem. Theory Comput.*, 2024, **20**, 2181–2191.

112 P. Elliott, F. Furche and K. Burke, *Excited states from time-dependent density functional theory*, in *Reviews in Computational Chemistry*, ed. K. B. Lipkowitz and T. R. Cundari, Wiley-VCH, New York, 2009, vol. 26, ch. 3, pp. 91–165.

113 M. Gronowski, TD-DFT benchmark: Excited states of atoms and atomic ions, *Comput. Theor. Chem.*, 2017, **1108**, 50–56.

114 D. Escudero, A. D. Laurent and D. Jacquemin, Time-dependent density functional theory: A tool to explore excited states, in *Handbook of Computational Chemistry*, ed. J. Leszczynski, A. Kaczmarek-Kedziera, T. Puzyn, M. G. Papadopoulos, H. Reis and M. K. Shukla, Springer International Publishing, Switzerland, 2nd edn, 2017, ch. 21, pp. 927–961.

115 J. Liang, X. Feng, D. Hait and M. Head-Gordon, Revisiting the performance of time-dependent density functional theory for electronic excitations: Assessment of 43 popular and recently developed functionals from rungs one to four, *J. Chem. Theory Comput.*, 2022, **18**, 3460–3473.

116 V. Mahamiya, P. Bhattacharyya and A. Shukla, Benchmarking Gaussian basis sets in quantum-chemical calculations of photoabsorption spectra of light atomic clusters, *ACS Omega*, 2022, **7**, 48261–48271.

117 A. Dreuw, J. L. Weisman and M. Head-Gordon, Long-range charge-transfer excited states in time-dependent density functional theory require non-local exchange, *J. Chem. Phys.*, 2003, **119**, 2943–2946.

118 A. Lange and J. M. Herbert, Simple methods to reduce charge-transfer contamination in time-dependent density-functional calculations of clusters and liquids, *J. Chem. Theory Comput.*, 2007, **3**, 1680–1690.

119 A. W. Lange, M. A. Rohrdanz and J. M. Herbert, Charge-transfer excited states in a π-stacked adenine dimer, as predicted using long-range-corrected time-dependent density functional theory, *J. Phys. Chem. B*, 2008, **112**, 6304–6308.

120 M. Gray, A. Mandal and J. M. Herbert, Revisiting the half-and-half functional, *J. Phys. Chem. A*, 2025, **129**, 3969–3982.

121 A. T. Wen and A. P. Hitchcock, Inner shell spectroscopy of $(\eta^5\text{-}C_5H_5)_2TiCl_2$, $(\eta^5\text{-}C_5H_5)_2TiCl_3$, and $TiCl_4$, *Can. J. Chem.*, 1993, **71**, 1632–1644.

122 J. M. Kasper, P. J. Lestrange, T. F. Stetina and X. Li, Modeling $L_{2,3}$-edge X-ray absorption spectroscopy with real-time exact two-component relativistic time-dependent density functional theory, *J. Chem. Theory Comput.*, 2018, **14**, 1998–2006.

123 G. Fronzoni, M. Stener, P. Decleva, F. Wang, T. Ziegler, E. van Lenthe and E. Baerends, Spin-orbit relativistic time dependent density functional theory calculations for the description of core electron excitations: $TiCl_4$ case study, *Chem. Phys. Lett.*, 2005, **416**, 56–63.

124 M. Casarin, P. Finetti, A. Vittadini, F. Wang and T. Ziegler, Spin-orbit relativistic time-dependent density functional calculations of the metal and ligand pre-edge XAS intensities of organotitanium complexes: $TiCl_4$, $Ti(\eta^5\text{-}C_5H_5)Cl_3$, and $Ti(\eta^5\text{-}C_5H_5)_2Cl_2$, *J. Phys. Chem. A*, 2007, **111**, 5270–5279.

125 M. Gray and J. M. Herbert, Comprehensive basis-set testing of extended symmetry-adapted perturbation theory and assessment of mixed-basis combinations to reduce cost, *J. Chem. Theory Comput.*, 2022, **18**, 2308–2330.

126 J. D. Bozek, K. H. Tan and G. M. Bancroft, High resolution gas phase photoabsorption spectra of $SiCl_4$ and $Si(CH_3)_4$ at the silicon L edges: Characterization and assignment of resonances, *Chem. Phys. Lett.*, 1987, **138**, 33–42.

127 G. Fronzoni, M. Stener, P. Decleva, M. de Simone, M. Coreno, P. Franceschi, C. Furlani and K. C. Prince, X-ray absorption spectroscopy of $VOCl_3$, CrO_2Cl_2, and MnO_3Cl: An experimental and theoretical study, *J. Phys. Chem. A*, 2009, **113**, 2914–2925.

128 M. Nakamura, M. Sasanuma, S. Sato, M. Watanabe, H. Yamashita, Y. Iguchi and A. Ejiri, Absorption structure near the $L_{\text{II,III}}$ edge of argon gas, *Phys. Rev. Lett.*, 1968, **21**, 1303–1305.

129 S. Bodeur and J. M. Esteva, Photoabsorption spectra of H_2S, CH_3SH and SO_2 near the sulfur K edge, *Chem. Phys.*, 1985, **100**, 415–427.

130 A. T. Wen, E. Ruehl and A. P. Hitchcock, Inner-shell excitation of organoiron compounds by electron impact, *Organometallics*, 1992, **11**, 2559–2569.

131 R. Brydson, L. A. J. Garvie, A. J. Craven, H. Sauer, F. Hofer and G. Cressey, $L_{2,3}$ edges of tetrahedrally coordinated d^0 transition-metal oxyanions XO_4^{n-}, *J. Phys.:Condens. Matter*, 1993, **5**, 9379–9392.

132 D. Danovich, C. M. Marian, T. Neuheuser, S. D. Peyerimhoff and S. Shaik, Spin-orbit coupling patterns induced by twist

and pyramidalization modes in C_2H_4: A quantitative study and a qualitative analysis, *J. Phys. Chem. A*, 1998, **102**, 5923–5936.

133 J. Tatchen and C. M. Marian, On the performance of approximate spin-orbit Hamiltonians in light conjugated molecules: The fine-structure splitting of HC_6H^+, NC_5H^+, and NC_4N^+, *Chem. Phys. Lett.*, 1999, **313**, 351–357.

134 E. Hudson, D. A. Shirley, M. Domke, G. Remmers, A. Puschmann, T. Mandel, C. Xue and G. Kaindl, High-resolution measurements of near-edge resonances in the core-level photoionization spectra of SF_6, *Phys. Rev. A:At., Mol., Opt. Phys.*, 1993, **47**, 361–373.

135 F. M. F. de Groot, Differences between L_3 and L_2 X-ray absorption spectra, *Phys. B*, 1995, **208–209**, 15–18.

136 K. Godehusen, T. Richter, P. Zimmermann and P. Wernet, Iron L-edge absorption spectroscopy of iron pentacarbonyl and ferrocene in the gas phase, *J. Phys. Chem. A*, 2017, **121**, 66–72.

137 A. P. Hitchcock, A. T. Wen and E. Rühl, Transition metal 2p excitation of organometallic compounds studied by electron energy loss spectroscopy, *Chem. Phys.*, 1990, **147**, 51–63.

138 M. Reiher, O. Salomon and B. A. Hess, Reparameterization of hybrid functionals based on energy differences of states of different multiplicity, *Theor. Chem. Acc.*, 2001, **107**, 48–55.

139 J. N. Harvey, DFT computation of relative spin-state energetics of transition metal compounds, *Struct. Bonding*, 2004, **112**, 151–183.

140 J. N. Harvey, On the accuracy of density functional theory in transition metal chemistry, *Annu. Rep. Prog. Chem., Sect. C:Phys. Chem.*, 2006, **102**, 203–226.

141 M. Radoń, Revisiting the role of exact exchange in DFT spin-state energetics of transition metal complexes, *Phys. Chem. Chem. Phys.*, 2014, **16**, 14479–14488.

142 G. Capano, T. J. Penfold, N. A. Besley, C. J. Milne, M. Reinhard, H. Rittmann-Frank, P. Glatzel, R. Abela, U. Rothlisberger, M. Chergui and I. Tavernelli, The role of Hartree-Fock exchange in the simulation of X-ray absorption spectra: A study of photoexcited $[Fe(bpy)_3]^{2+}$, *Chem. Phys. Lett.*, 2013, **580**, 179–184.

143 C.-M. Jiang, *Charge Carrier Dynamics in Transition Metal Oxides Studied by Femtosecond Transient Extreme Ultraviolet Absorption Spectroscopy*, *PhD thesis*, University of California, Berkeley, 2015.

144 A. Kubas, M. Verkamp, J. Vura-Weis, F. Neese and D. Maganas, Restricted open-shell configuration interaction singles study on M- and L-edge X-ray absorption spectroscopy of solid chemical systems, *J. Chem. Theory Comput.*, 2018, **14**, 4320–4334.

145 Ohio Supercomputer Center, **https://osc.edu/ark:/19495/f5s1ph73** (accessed 2025-07-08).